

Slow nonisothermal flows: numerical and asymptotic analysis of the Boltzmann equation

O. A. Rogozin*

Abstract

In memory of Oskár Gavriilovich Friedländer (1939–2015)

Slow flows of a slightly rarefied gas under high thermal stresses are considered. The correct fluid-dynamic description of this class of flows is based on the Kogan–Galkin–Friedlander equations, containing some non-Navier–Stokes terms in the momentum equation. Appropriate boundary conditions are determined from the asymptotic analysis of the Knudsen layer on the basis of the Boltzmann equation. Boundary conditions up to the second order of the Knudsen number are studied. Some two-dimensional examples are examined for their comparative analysis. The fluid-dynamic results are supported by numerical solution of the Boltzmann equation obtained by the Tcheremissine’s projection-interpolation discrete-velocity method extended for nonuniform grids. The competition pattern between the first- and the second-order nonlinear thermal-stress flows has been obtained for the first time.

Keywords: Boltzmann equation, Kogan–Galkin–Friedlander equations, nonlinear thermal-stress flow, projection method, OpenFOAM

1 Introduction

From 1969 to 1974, Oscar Gavriilovich Friedlander (1939–2015) together with Vladlen Sergeevich Galkin (b. 1932) under the guidance of Mikhail Naumovich Kogan (1925–2011) developed the theory of *slow nonisothermal slightly rarefied gas flows* [1, 2, 3, 4, 5]. Slowness should be understood as the smallness of the Mach number ($Ma \ll 1$), nonisothermality as the presence of significant temperature gradient in the gas ($\nabla \log T \sim 1$), and slightly rarefied means the smallness of the Knudsen number ($Kn \ll 1$). The attempt to take into consideration the impact of thermal stress on the gas motion through the analysis of the Burnett approximation was the main impetus of the mentioned works. Despite the Burnett terms are of the second order of the Knudsen number, they become comparable to the Newtonian viscous stresses in the case $Ma \sim Kn$ (the Reynolds number is about unity). Thus, the Navier–Stokes equations are incorrect to describe slow nonisothermal flows.

The correct set of fluid-dynamic-type equations was first obtained in [1]. There is no widely accepted term in the literature, so the author proposes to call them as the *Kogan–Galkin–Friedlander* or *KGF equations* [5]. In the first papers [1, 2], these equations have been obtained the simplest way, based on the Chapman–Enskog expansion, later from the Hilbert expansion [4]. The most general formulation of the time-dependent KGF equations for the mixture of gases can be found in [6].

In addition to the viscosity and thermal conductivity coefficients, the KGF equations contain some *thermal-stress transport coefficients*. For some molecular potentials they were first calculated using the Sonine (associated Laguerre) polynomials [7, 8]. For a hard-sphere gas, more accurate values were computed using the direct numerical solution of corresponding integral equations [9, 10, 11].

The nonlinear nature of the thermal stresses in the KGF equations leads to the phenomenon of gas convection under their action (*nonlinear thermal-stress convection*) [2]. This type of convection takes place

*oleg.rogozin@phystech.edu, Moscow Institute of Physics and Technology, 9 Institutskiy per., Dolgoprudny, Moscow Region, 141700, Russian Federation

in the absence of external forces and may occur between uniformly heated bodies. Nonlinear thermal stresses have also an influence on the process of heat transfer [12]. After many years of work, Oscar Friedlander and his group succeeded in confirming the theory of slow nonisothermal flows experimentally [13, 14]. At the same time, thanks to the development of computer technology, some applied problems were analyzed numerically using the KGF and kinetic equations: on the basis of model equations [15, 16, 17, 18, 19] and the direct simulation Monte Carlo (DSMC) method [20, 21].

For small Knudsen numbers, and especially slow flows, the classical DSMC method is extremely expensive. Many specialized stochastic schemes have been proposed in recent years [22, 23]. Deterministic methods for the Boltzmann equation are also very promising [24, 25]. However, the computational difficulties have not been overcome completely up to date. For this reason, there are no numerical examples of the nonlinear thermal-stress flows on the basis of the Boltzmann equation, which require high accuracy of the numerical method, in the literature. In addition, these flows cannot be observed in one-dimensional problems. A high-accuracy analysis of the Knudsen layer is also a cumbersome task [26], especially around curved surfaces [27]. Slow flows with a wide temperature range impose additional requirements on the grid in the velocity space: the distribution function of both cold and hot gas should be approximated equally well. It can be satisfied, when the grid has a large volume, but refines for small molecular velocities. The extension of the Tcheremissine's projection-interpolation discrete-velocity method [28, 29, 30, 31] for nonuniform grids [32] based on the methodology of multi-point projection [33] can effectively solve the considered class of problems.

Asymptotic analysis of the Boltzmann equation for slow nonisothermal flows shows that the steady-state heat-conduction equation does not correctly describe a rarefied gas in the continuum limit ($\text{Kn} \rightarrow 0$) [34]. This fact is also confirmed by numerical analysis [9]. It turns out that infinitesimal velocity field has a finite impact on the temperature field. This asymptotic behavior has been called the *ghost effect* [10, 11]. Some mathematical questions of existence and stability of solutions to the KGF equations are discussed in [35, 36].

So far, the KGF equations were solved numerically only with the thermal-creep boundary conditions. They are natural for the asymptotic equations of the leading order; however, the solution can be improved if some boundary conditions of the following order are exploited, such as temperature and speed jumps, thermal-stress slip, as well as those second-order terms that comprise the curvature of the boundary surface. This is possible since the above mentioned conditions depend only on the leading-order solution and some of its derivatives.

2 Basic equations

First of all, turn to dimensionless variables. Let L be the reference length, $T^{(0)}$ and $p^{(0)}$ be the reference temperature and pressure of the gas. Then the macroscopic variables take the following form: $TT^{(0)}$ is the temperature, $pp^{(0)}$ is the pressure, $\rho p^{(0)}/RT^{(0)}$ is the density, $v_i(2RT^{(0)})^{1/2}$ is the velocity. The distribution function $f(x_i, \zeta_i)(2p^{(0)})/(2RT^{(0)})^{5/2}$ is defined in the physical $x_i L$ and velocity $\zeta_i(2RT^{(0)})^{1/2}$ spaces. The specific gas constant $R = k_B/m$, where k_B is the Boltzmann constant, m is the mass of a molecule. The Knudsen number $\text{Kn} = \ell^{(0)}/L$ is defined using the reference length free path

$$\ell^{(0)} = \frac{k_B T^{(0)}}{\sqrt{2\pi} d_m^2 p^{(0)}}, \quad (1)$$

where d_m coincides with the diameter of hard-sphere molecules.

In the presence of external forces $F_i(2RT^{(0)})/L$, the dimensionless time-independent Boltzmann equation is

$$\zeta_i \frac{\partial f}{\partial x_i} + F_i \frac{\partial f}{\partial \zeta_i} = \frac{1}{k} J(f, f), \quad (2)$$

where the collision integral

$$J(f, g) = \frac{1}{2} \int (f' g'_* + g' f'_* - f g_* - g f_*) B d\Omega(\alpha) d\zeta_* \quad (3)$$

and $k = \sqrt{\pi}Kn/2$. $\Omega(\alpha)$ is the solid angle in the direction of the unit vector α , B is the functional of the intermolecular potential. For a hard-sphere gas,

$$B = \frac{|\alpha_i(\zeta_{i*} - \zeta_i)|}{4\sqrt{2\pi}}. \quad (4)$$

The macroscopic variables are expressed through the moments of the distribution function:

$$\rho = \int f d\zeta, \quad v_i = \frac{1}{\rho} \int \zeta_i f d\zeta, \quad T = \frac{2}{3\rho} \int (\zeta_i - v_i)^2 f d\zeta, \quad p = \rho T. \quad (5)$$

The boundary conditions of diffuse reflection are specified as follows:

$$f(\zeta_i n_i > 0) = \frac{\sigma_B}{(\pi T_B)^{3/2}} \exp\left(-\frac{\zeta_i^2}{T_B}\right), \quad \sigma_B = -2 \left(\frac{\pi}{T_B}\right)^{1/2} \int_{\zeta_i n_i < 0} \zeta_j n_j f d\zeta, \quad (6)$$

where n_i is the unit vector normal to the boundary, directed into gas, T_B and v_{Bi} are the boundary temperature and velocity. For time-independent problems, it is assumed that $v_{Bi} n_i = 0$.

3 Asymptotic analysis

This section summarizes the main results of the asymptotic theory of slow nonisothermal flows based on the Hilbert expansion. The notation introduced in [10, 11] is used. For simplicity, only the hard-sphere molecular model is considered.

For small k , the solution of time-independent Boltzmann equation can be separated into different length scales. Consider the following form:

$$f = f_H + f_K, \quad (7)$$

where f_H is the fluid-dynamic part of the solution on the scale $O(1)$, f_K is the Knudsen-layer correction on the scale $O(k)$. This separation is clear when f_K decreases faster than any inverse power of the distance from the boundary. Nonlinear perturbation theory provides f_H that depends only on the macroscopic variables and their derivatives, but f_H does not possess enough degrees of freedom to satisfy the diffuse-reflection boundary condition (6). Numerical solution of the Knudsen-layer problem yields f_K , as well as the boundary conditions for f_H .

3.1 Fluid-dynamic part of the solution

The distribution function f_H and the macroscopic variables $h_H = \rho_H, v_{iH}, T_H, \dots$ can be expanded in a power series of k :

$$f_H = f_{H0} + f_{H1}k + f_{H2}k^2 + \dots, \quad h_H = h_{H0} + h_{H1}k + h_{H2}k^2 + \dots. \quad (8)$$

We look for a solution of the Boltzmann equation under the assumptions that $\partial f_H / \partial x_i = O(f_H)$ (the Hilbert expansion), $v_{iH0} = 0$ (slow flows), $F_{iH0} = F_{iH1} = 0$ (a weak field of external forces). Substituting (8) in the Boltzmann equation (2) and collecting terms of the same order of k , we obtain a system of integro-differential equations, for which the following solvability conditions must be satisfied: in the zeroth order

$$\frac{\partial p_{H0}}{\partial x_i} = 0; \quad (9)$$

in the first order

$$\frac{\partial}{\partial x_i} \left(\frac{u_{iH1}}{T_{H0}} \right) = 0, \quad (10)$$

$$\frac{\partial p_{H1}}{\partial x_i} = 0, \quad (11)$$

$$\frac{\partial u_{iH1}}{\partial x_i} = \frac{\gamma_2}{2} \frac{\partial}{\partial x_i} \left(\sqrt{T_{H0}} \frac{\partial T_{H0}}{\partial x_i} \right); \quad (12)$$

for $p_{H1} = 0$, in the second order

$$\frac{\partial}{\partial x_i} \left(\frac{u_{iH2}}{T_{H0}} \right) = \frac{u_{iH1}}{T_{H0}} \frac{\partial}{\partial x_i} \left(\frac{T_{H1}}{T_{H0}} \right), \quad (13)$$

$$\begin{aligned} \frac{\partial}{\partial x_j} \left(\frac{u_{iH1} u_{jH1}}{T_{H0}} \right) - \frac{\gamma_1}{2} \frac{\partial}{\partial x_j} \left[\sqrt{T_{H0}} \left(\frac{\partial u_{iH1}}{\partial x_j} + \frac{\partial u_{jH1}}{\partial x_i} - \frac{2}{3} \frac{\partial u_{kH1}}{\partial x_k} \delta_{ij} \right) \right] \\ - \frac{\bar{\gamma}_7}{T_{H0}} \frac{\partial T_{H0}}{\partial x_i} \frac{\partial T_{H0}}{\partial x_j} \left(\frac{u_{jH1}}{\gamma_2 \sqrt{T_{H0}}} - \frac{1}{4} \frac{\partial T_{H0}}{\partial x_j} \right) = -\frac{1}{2} \frac{\partial p_{H2}^\dagger}{\partial x_i} + \frac{p_{H0}^2 F_{iH2}}{T_{H0}}, \end{aligned} \quad (14)$$

$$\frac{\partial u_{iH2}}{\partial x_i} = \frac{\gamma_2}{2} \frac{\partial^2}{\partial x_i^2} \left(T_{H1} \sqrt{T_{H0}} \right). \quad (15)$$

The following notation is introduced here: $u_{iH1} = p_{H0} v_{iH1}$, $u_{iH2} = p_{H0} v_{iH2}$, and

$$p_{H2}^\dagger = p_{H0} p_{H2} + \frac{2\gamma_3}{3} \frac{\partial}{\partial x_k} \left(T_{H0} \frac{\partial T_{H0}}{\partial x_k} \right) - \frac{\bar{\gamma}_7}{6} \left(\frac{\partial T_{H0}}{\partial x_k} \right)^2. \quad (16)$$

Equations (10), (12), (14) for T_{H0} , u_{iH1} , p_{H2}^\dagger are proposed to be called *Kogan–Galkin–Friedlander* or *KGF equations* [5]. They contain a thermal-stress term, which is absent in the Navier–Stokes equations. Comparing it with $p_{H0}^2 F_{iH2}/T_{H0}$, we find that

$$k^2 \frac{\bar{\gamma}_7}{p_{H0}^2} \frac{\partial T_{H0}}{\partial x_i} \frac{\partial T_{H0}}{\partial x_j} \left(\frac{u_{jH1}}{\gamma_2 \sqrt{T_{H0}}} - \frac{1}{4} \frac{\partial T_{H0}}{\partial x_j} \right). \quad (17)$$

is the force acting on unit mass of the gas. It occurs when the isothermal surfaces are not parallel, i.e.,

$$e_{ijk} \frac{\partial T_{H0}}{\partial x_j} \frac{\partial}{\partial x_k} \left(\frac{\partial T_{H0}}{\partial x_l} \right)^2 \neq 0. \quad (18)$$

The Levi-Civita symbol e_{ijk} is used in (18). The gas motion driven by this force is called now the *nonlinear thermal-stress flow* [10, 11].

Note that p_{H2}^\dagger is not included directly in the equation of state and is therefore determined up to a constant. Since the term $\partial p_{H2}^\dagger / \partial x_i$ is included in the system as the pressure in the Navier–Stokes equations for incompressible gas, the corresponding numerical methods are used to solve the KGF equations.

The dimensionless transport coefficients for a hard-sphere gas:

$$\begin{aligned} \gamma_1 &= 1.270042427, & \gamma_2 &= 1.922284066, \\ \gamma_3 &= 1.947906335, & \bar{\gamma}_7 &= 1.758705. \end{aligned}$$

The first two of them correspond, respectively, to the viscosity μ and the thermal conductivity λ of the gas,

$$\mu = \gamma_1 \sqrt{T_{H0}} \frac{p^{(0)} L}{\sqrt{2RT^{(0)}}} k, \quad \lambda = \frac{5\gamma_2}{2} \sqrt{T_{H0}} \frac{p^{(0)} RL}{\sqrt{2RT^{(0)}}} k. \quad (19)$$

The coefficient γ_3 is included in the thermal-stress expressions that create nonuniform pressure distribution in the gas, but not the driving force. Since $\bar{\gamma}_7$ is positive, nonlinear thermal-stress flow is opposite to the temperature gradient.

3.2 Knudsen layer and boundary conditions

The diffuse-reflection condition (6) can be satisfied, if we assume that f_K decreases exponentially on the scale of the mean free path in the proximity of a boundary:

$$kn_i \frac{\partial f_K}{\partial x_i} = O(f_K), \quad k \rightarrow 0, \quad (20)$$

$$f_K = o(\eta^{-m}), \quad \eta \rightarrow \infty, \quad m \in \mathbb{N}. \quad (21)$$

Here, the natural orthogonal Knudsen-layer variables are introduced:

$$x_i = k\eta n_i(\chi_1, \chi_2) + x_{Bi}(\chi_1, \chi_2), \quad (22)$$

where x_{Bi} is the boundary surface, η is the stretched coordinate along the normal vector n_i , χ_1 and χ_2 are coordinates within the surface $\eta = \text{const}$. Then f_K satisfies

$$\zeta_i n_i \frac{\partial f_K}{\partial \eta} = 2J(f_H, f_K) + J(f_K, f_K) - k\zeta_i \left(\frac{\partial \chi_1}{\partial x_i} \frac{\partial f_K}{\partial \chi_1} + \frac{\partial \chi_2}{\partial x_i} \frac{\partial f_K}{\partial \chi_2} \right). \quad (23)$$

The fluid-dynamic part of the zeroth-order solution is Maxwellian

$$f_{H0} = \frac{\rho_{H0}}{(\pi T_{H0})^{3/2}} \exp\left(-\frac{\zeta_i^2}{T_{H0}}\right), \quad (24)$$

which satisfies (6) if

$$T_{H0} = T_{B0}; \quad (25)$$

therefore, $f_{K0} = 0$. Using the expansions

$$f_K = f_{K1}k + f_{K2}k^2 + \dots, \quad (26)$$

$$f_H = (f_{H0})_0 + \left[(f_{H1})_0 + \eta \left(\frac{\partial f_{H0}}{\partial x_i} \right)_0 n_i \right] k + \dots, \quad (27)$$

where $(\dots)_0$ denotes the value of on the boundary ($\eta = 0$), the equations for f_{K1} and f_{K2} are

$$\zeta_i n_i \frac{\partial f_{K1}}{\partial \eta} = 2J[(f_{H0})_0, f_{K1}], \quad (28)$$

$$\begin{aligned} \zeta_i n_i \frac{\partial f_{K2}}{\partial \eta} = & 2J[(f_{H0})_0, f_{K2}] - \zeta_i \left[\left(\frac{\partial \chi_1}{\partial x_i} \right)_0 \frac{\partial f_{K1}}{\partial \chi_1} + \left(\frac{\partial \chi_2}{\partial x_i} \right)_0 \frac{\partial f_{K1}}{\partial \chi_2} \right] \\ & + 2J \left[(f_{H1})_0 + \eta \left(\frac{\partial f_{H0}}{\partial x_i} \right)_0 n_i, f_{K1} \right] + J(f_{K1}, f_{K1}). \end{aligned} \quad (29)$$

Under appropriate boundary conditions in the half space $\eta > 0$, there exists a unique solution of the one-dimensional linearized (about Maxwellian f_{H0} on the boundary) Boltzmann equation (28) if and only if the boundary values of T_{H1} and $u_{jH1}(\delta_{ij} - n_i n_j)$ take specific values [37, 38]. A similar statement holds for (29) and the boundary values T_{H2} , $u_{jH2}(\delta_{ij} - n_i n_j)$.

The homogeneous equation (28) leads to the following boundary conditions and Knudsen-layer corrections:

$$\frac{1}{\sqrt{T_{B0}}} \left[\begin{array}{c} (u_{jH1} - u_{Bj2}) \\ u_{jK1} \end{array} \right] (\delta_{ij} - n_i n_j) = - \left(\frac{\partial T_{H0}}{\partial x_j} \right)_0 (\delta_{ij} - n_i n_j) \left[\frac{K_1}{\frac{1}{2} Y_1(\tilde{\eta})} \right], \quad (30)$$

$$\left[\begin{array}{c} u_{jH1} \\ u_{jK1} \end{array} \right] n_j = 0, \quad (31)$$

$$\frac{p_{H0}}{T_{B0}} \left[\begin{array}{c} T_{H1} - T_{B1} \\ T_{K1} \\ T_{B0}^2 \rho_{K1} \end{array} \right] = \left(\frac{\partial T_{H0}}{\partial x_j} \right)_0 n_j \left[\begin{array}{c} d_1 \\ \Theta_1(\tilde{\eta}) \\ p_{H0} \Omega_1(\tilde{\eta}) \end{array} \right], \quad (32)$$

where $\tilde{\eta} = \eta p_{H0}/T_{B0}$. The coefficients d_1 and K_1 correspond to the temperature jump and thermal creep, respectively. For a hard-sphere gas, [39, 40, 41]

$$d_1 = 2.40014, \quad K_1 = -0.64642. \quad (33)$$

Since $K_1 < 0$, the direction of the thermal creep coincides with the direction of the temperature gradient of the boundary surface. The functions $Y_1(\eta)$, $\Theta_1(\eta)$, $\Omega_1(\eta)$ decrease exponentially with η and are tabulated for a hard-sphere gas in [39, 40, 10, 11, 41].

In contrast to (28), equation (29) is inhomogeneous. In the absence of the last two nonlinear terms, this problem is well studied, as appears in the asymptotic analysis of the linearized Boltzmann equation, and leads to the following boundary conditions and Knudsen-layer corrections:

$$\begin{aligned} & \frac{1}{\sqrt{T_{B0}}} \left[\frac{(u_{jH2} - u_{Bj2})}{u_{jK2}} \right] (\delta_{ij} - n_i n_j) = - \frac{\sqrt{T_{B0}}}{p_{H0}} \left(\frac{\partial u_{jH1}}{\partial x_k} \right)_0 (\delta_{ij} - n_i n_j) n_k \left[\frac{k_0}{Y_0(\tilde{\eta})} \right] \\ & - \frac{T_{B0}}{p_{H0}} \left(\frac{\partial^2 T_{H0}}{\partial x_j \partial x_k} \right)_0 (\delta_{ij} - n_i n_j) n_k \left[\frac{a_4}{Y_{a4}(\tilde{\eta})} \right] - \bar{\kappa} \frac{T_{B0}}{p_{H0}} \left(\frac{\partial T_{H0}}{\partial x_j} \right)_0 (\delta_{ij} - n_i n_j) \left[\frac{a_5}{Y_{a5}(\tilde{\eta})} \right] \end{aligned} \quad (34)$$

$$\begin{aligned} & - \kappa_{jk} \frac{T_{B0}}{p_{H0}} \left(\frac{\partial T_{H0}}{\partial x_k} \right)_0 (\delta_{ij} - n_i n_j) \left[\frac{a_6}{Y_{a6}(\tilde{\eta})} \right] - \frac{\partial T_{B1}}{\partial x_j} (\delta_{ij} - n_i n_j) \left[\frac{K_1}{\frac{1}{2} Y_1(\tilde{\eta})} \right], \\ & \frac{1}{\sqrt{T_{B0}}} \left[\frac{(u_{jH2} - u_{Bj2})}{u_{jK2}} \right] n_j = \\ & - \frac{T_{B0}}{p_{H0}} \left[\left(\frac{\partial^2 T_{H0}}{\partial x_i \partial x_j} \right)_0 n_i n_j + 2\bar{\kappa} \left(\frac{\partial T_{H0}}{\partial x_i} \right)_0 n_i \right] \left[\frac{\frac{1}{2} \int_0^\infty Y_1(\eta_0) d\eta_0}{\frac{1}{2} \int_0^\infty Y_1(\eta_0) d\eta_0} \right], \end{aligned} \quad (35)$$

$$\begin{aligned} & \frac{p_{H0}}{T_{B0}} \left[\frac{T_{H2} - T_{B2}}{T_{K2}^2 \rho_{K2}} \right] = \left(\frac{\partial T_{H1}}{\partial x_j} \right)_0 n_j \left[\frac{d_1}{p_{H0} \Omega_1(\tilde{\eta})} \right] \\ & + \frac{T_{B0}}{p_{H0}} \left(\frac{\partial^2 T_{H0}}{\partial x_i \partial x_j} \right)_0 n_i n_j \left[\frac{d_3}{p_{H0} \Omega_3(\tilde{\eta})} \right] + \bar{\kappa} \frac{T_{B0}}{p_{H0}} \left(\frac{\partial T_{H0}}{\partial x_i} \right)_0 n_i \left[\frac{d_5}{p_{H0} \Omega_5(\tilde{\eta})} \right], \end{aligned} \quad (36)$$

where $\bar{\kappa}/L = (\kappa_1 + \kappa_2)/2L$ is the mean curvature of the boundary surface. The principal curvatures, κ_1/L and κ_2/L , become negative when the corresponding center of curvature lies on the side of gas. The dimensionless curvature tensor $\kappa_{ij} = \kappa_1 l_i l_j + \kappa_2 m_i m_j$ is expressed in terms of the direction cosines of the principal directions, l_i and m_i .

The coefficient a_4 corresponds to the second-order thermal-stress slip. For a hard-sphere gas, [42, 41]

$$a_4 = 0.0331. \quad (37)$$

Since $a_4 > 0$, there is a phenomenon of negative thermophoresis [42]. The coefficients in front of $\bar{\kappa}$ and κ_{ij} are computed recently [27, 41]:

$$a_5 = 0.23353, \quad a_6 = -1.99878, \quad d_3 = 0.4993, \quad d_5 = 4.6180. \quad (38)$$

Functions $Y_{a4}(\eta)$, $Y_{a5}(\eta)$, $Y_{a6}(\eta)$, $\Theta_3(\eta)$, $\Omega_3(\eta)$, $\Theta_5(\eta)$, $\Omega_5(\eta)$ also decrease exponentially with η and are tabulated for a hard-sphere gas in [42, 10, 11, 27, 41].

The last two terms in (29) result in the additional nonlinear terms in (34) and (36):

$$\frac{1}{p_{H0}^2} \left(\frac{\partial T_{H0}}{\partial x_j} (\delta_{ij} - n_i n_j) \right)_0 \left(\frac{\partial T_{H0}}{\partial x_k} n_k \right)_0, \quad \frac{1}{p_{H0}^2} \left(\frac{\partial T_{H0}}{\partial x_i} n_i \right)_0^2; \quad (39)$$

however, the complete solution of this inhomogeneous Knudsen-layer problem for a hard-sphere gas is not presented in the literature. For the model Krook–Welanders equation [43, 44], numerical analysis of the second term (from (39)) is presented in [45].

3.3 Technique of using the next-order boundary conditions

The next-order equations for T_{H1} , v_{iH2} , p_{H3} is cumbersome and have not been obtained in the general form for an arbitrary molecular potential. Therefore, numerical analysis of slow slightly rarefied flows is usually

based on the KGF equations (10), (12), (14) with the leading-order boundary conditions (25), (30), (31). However, the asymptotic solution can be improved by introducing the known next-order boundary conditions. For example, it is possible to calculate the temperature field $T_H = T_{H0} + T_{H1}k + O(k^2)$ from the equation

$$\frac{1}{k} \frac{\partial u_{iH}}{\partial x_i} = \frac{\gamma_2}{2} \frac{\partial}{\partial x_i} \left(\sqrt{T_H} \frac{\partial T_H}{\partial x_i} \right) + O(k^2), \quad (40)$$

which is obtained from (12) and (15), with the boundary condition

$$T_H = T_B + d_1 \frac{T_{B0}}{p_{H0}} \left(\frac{\partial T_H}{\partial x_j} \right)_0 n_j k + O(k^2), \quad (41)$$

which is obtained from (25) and (32). Since u_{iH2} is unknown, the temperature field T_H is calculated with the accuracy $O(k)$, but have the accuracy $O(k^2)$ on the boundary. The derivative of T_H is used in (41) instead of $\partial T_{H0}/\partial x_j$; therefore, the temperature jump of the next-order boundary condition is taken into account. Similarly, the velocity jump can be considered:

$$u_{iH} = u_{Bi1}k - \left[K_1 \sqrt{T_{B0}} \left(\frac{\partial T_{H0}}{\partial x_j} \right)_0 + k_0 \frac{T_{B0}}{p_{H0}} \left(\frac{\partial u_{jH}}{\partial x_k} \right)_0 n_k \right] (\delta_{ij} - n_i n_j) k + O(k^2). \quad (42)$$

The terms from (34) and (36) that contain the second derivative of T_{H0} as well as $\bar{\kappa}$ and κ_{ij} can be included in the boundary conditions in the same way. The boundary condition for the normal component of the velocity (35) is incompatible with the equation (10) and is therefore not used.

The fields T_H and u_{iH} obtained as described above describe the behavior of a rarefied gas qualitatively better, because the additional boundary effects are taken into consideration. Hence, one can also hope that they approximate the exact solution quantitatively better.

To calculate the second derivative of T_{H0} in the normal direction, it is convenient to use the following transformation of (12) and (30):

$$\frac{\partial^2 T_{H0}}{\partial x_i \partial x_j} n_i n_j + 2\bar{\kappa} \frac{\partial T_{H0}}{\partial x_i} n_i = -\frac{\partial^2 T_{H0}}{\partial \chi_\alpha^2} - \frac{1}{2T_{H0}} \left[\left(\frac{\partial T_{H0}}{\partial x_i} n_i \right)^2 + \left(1 + \frac{4K_1}{\gamma_2} \right) \left(\frac{\partial T_{H0}}{\partial \chi_\alpha} \right)^2 \right], \quad (43)$$

where each pair of repeated indices $\alpha = 1, 2$ implies summation over them, and $|\partial \chi_\alpha / \partial x_i| = 1$.

3.4 Computational implementation

To solve the KGF equations (10), (12), (14), we employ the finite-volume method and the SIMPLE algorithm for pressure-velocity coupling [21]. The boundary conditions like (41) lead to the third-type boundary-value problem, the solution of which requires additional measures to maintain stability of the numerical scheme. The boundary temperature can become negative for large values of $n_j \partial T_{H0} / \partial x_j$. To avoid this, it is usually sufficient to introduce a relaxation factor for the boundary conditions. Moreover, the considered boundary-value problem has a solution in the limited range $k < k_{\max}$. The larger the temperature difference in the problem, the less k_{\max} . However, the solution of KGF equations is anyway unable to approximate the exact kinetic solution adequately for larger k_{\max} .

3.5 Continuum limit

In the classical fluid-dynamics, the Navier-Stokes equations ($\bar{\gamma}_7 = 0$ with the boundaries at rest ($v_{Bi} = 0$) and the conditions without thermal creep ($K_1 = 0$) lead to the zero velocity field $v_{iH1} = 0$ and the heat-conduction equation

$$\frac{\partial}{\partial x_i} \left(\sqrt{T_{H0}} \frac{\partial T_{H0}}{\partial x_i} \right) = 0. \quad (44)$$

In the general case, the correct temperature distribution in the continuum limit ($k \rightarrow 0$) is obtained from the KGF equations with appropriate boundary conditions. It will coincide with the solution of (44) only for a narrow class of problems.

In the continuum world ($k = 0$), there are no quantities like u_{iH1} and p_{H2}^\dagger ; nevertheless, infinitesimal velocity field v_i produce a finite effect on T . Such asymptotic behavior is called the ghost effect [10, 11].

4 Method of solving the Boltzmann equation

In the present work, the Boltzmann equation, written in such a dimensionless form that the mean free path is the reference length

$$\frac{\partial f}{\partial t} + \zeta_i \frac{\partial f}{\partial x_i} = J(f), \quad (45)$$

is solved numerically using the second-order symmetric splitting into the transport equation

$$\frac{\partial f}{\partial t} + \zeta_i \frac{\partial f}{\partial x_i} = 0, \quad (46)$$

for which the finite-volume method with an explicit second-order TVD-scheme is employed, and into the space-homogeneous Boltzmann equation

$$\frac{\partial f}{\partial t} = J(f), \quad (47)$$

for which the projection-interpolation discrete-velocity method for non-uniform velocity grids is employed. The brief description of the latter one is presented below.

4.1 Discretization of the velocity space

Let regular velocity grid $\mathcal{V} = \{ \zeta_\gamma : \gamma \in \Gamma \}$ is constructed in such a way that the cubature over the molecular velocity space ζ is expressed as a weighted sum

$$\int F(\zeta) d\zeta \approx \sum_{\gamma \in \Gamma} F_\gamma w_\gamma = \sum_{\gamma \in \Gamma} \hat{F}_\gamma, \quad \sum_{\gamma \in \Gamma} w_\gamma = V_\Gamma, \quad F_\gamma = F(\zeta_\gamma), \quad (48)$$

where $F(\zeta)$ is an arbitrary integrable function, V_Γ is the total volume of the velocity grid, Γ is some index set. Then, the eight-dimensional cubature formula in the space (ω, ζ, ζ_*) can be written as

$$\int F(\omega, \zeta, \zeta_*) d\Omega(\omega) d\zeta d\zeta_* \approx \frac{4\pi V_\Gamma^2}{\sum_{\nu \in \mathcal{N}} w_{\alpha_\nu} w_{\beta_\nu}} \sum_{\nu \in \mathcal{N}} F(\omega_\nu, \zeta_{\alpha_\nu}, \zeta_{\beta_\nu}) w_{\alpha_\nu} w_{\beta_\nu}, \quad (49)$$

where $F(\omega, \zeta, \zeta_*)$ is also an arbitrary integrable function. $\alpha_\nu \in \Gamma$, $\beta_\nu \in \Gamma$, and $\omega_\nu \in S^2 = \{ \omega \in \mathbb{R}^3 : |\omega| = 1 \}$ are obtained from some equal-weight cubature rule, $\mathcal{N} \subset \mathbb{N}$ is its index set. Note that the numerical integration in (49) is carried out over the discrete spectrum of (ζ, ζ_*) and continuous spectrum of ω .

The collision integral written in the symmetrized form

$$J(f_\gamma) = \frac{1}{4} \int [\delta(\zeta - \zeta_\gamma) + \delta(\zeta_* - \zeta_\gamma) - \delta(\zeta' - \zeta_\gamma) - \delta(\zeta'_* - \zeta_\gamma)] (f' f'_* - f f_*) B d\Omega(\omega) d\zeta d\zeta_*, \quad (50)$$

where $\delta(\zeta)$ is the Dirac delta function in \mathbb{R}^3 , has the following discrete analogue:

$$\hat{J}_\gamma(\hat{f}_\gamma) = \frac{\pi V_\Gamma^2}{\sum_{\nu \in \mathcal{N}} w_{\alpha_\nu} w_{\beta_\nu}} \sum_{\nu \in \mathcal{N}} (\delta_{\alpha_\nu \gamma} + \delta_{\beta_\nu \gamma} - \delta_{\alpha'_\nu \gamma} - \delta_{\beta'_\nu \gamma}) \left(\frac{w_{\alpha_\nu} w_{\beta_\nu}}{w_{\alpha'_\nu} w_{\beta'_\nu}} \hat{f}_{\alpha'_\nu} \hat{f}_{\beta'_\nu} - \hat{f}_{\alpha_\nu} \hat{f}_{\beta_\nu} \right) B_\nu, \quad (51)$$

where $\delta_{\zeta\gamma}$ is the Kronecker delta. In the general case, $\zeta_{\alpha'_\nu}$ and $\zeta_{\beta'_\nu}$ are not in \mathcal{V} ; therefore, quantities $\hat{f}_{\alpha'_\nu}$, $\hat{f}_{\beta'_\nu}$, w_{α_ν} , w_{β_ν} and functions $\delta_{\alpha'_\nu \gamma}$, $\delta_{\beta'_\nu \gamma}$ have to be defined in some way.

The Maxwell distribution is approximated as follows:

$$\hat{f}_{M\gamma} = \rho \left[\sum_{\varsigma \in \Gamma} w_{\varsigma} \exp \left(-\frac{(\zeta_{\varsigma} - \mathbf{v})^2}{T} \right) \right]^{-1} w_{\gamma} \exp \left(-\frac{(\zeta_{\gamma} - \mathbf{v})^2}{T} \right). \quad (52)$$

4.2 Projection-interpolation technique

If the velocities after collision, $\zeta_{\alpha'_{\nu}} \notin \mathcal{V}$ and $\zeta_{\beta'_{\nu}} \notin \mathcal{V}$, are replaced with the nearest grid velocities, $\zeta_{\lambda_{\nu}} \in \mathcal{V}$ and $\zeta_{\mu_{\nu}} \in \mathcal{V}$, the discrete collision integral (51) is not strictly conservative, and the discrete Maxwellian (52) is not the equilibrium state. To resolve these issues, two special procedures are applied in the projection-interpolation method. First, $\zeta_{\alpha'_{\nu}}$ is projected to a set of grid velocities $\{\zeta_{\lambda_{\nu}+s_a} : a \in \Lambda\} \subset \mathcal{V}$ in the following way:

$$\delta_{\alpha'_{\nu}\gamma} = \sum_{a \in \Lambda} r_{\lambda_{\nu},a} \delta_{\lambda_{\nu}+s_a,\gamma}, \quad (53)$$

where the index set $\Lambda = \{a : r_{\lambda_{\nu},a} \neq 0\} \subset \mathbb{Z}$. The set of displacement rules $\mathcal{S} = \{s_a : a \in \Lambda\}$ is called the *projection stencil*.

The expression (53) can be formally regarded as an approximate solution of the equation $\phi = \delta(\zeta' - \zeta_{\gamma})$ in the space of delta functions $\{\delta(\zeta - \zeta_{\gamma}) : \zeta_{\gamma} \in \mathcal{N}\}$ by the projection Petrov–Galerkin method onto a linear span of functions $\psi_s(\zeta)$:

$$\int \psi_s(\zeta_{\gamma}) \left(\delta(\zeta' - \zeta_{\gamma}) - \sum_{a \in \Lambda} r_{\lambda_{\nu},a} \delta(\zeta_{\lambda_{\nu}+s_a} - \zeta_{\gamma}) \right) d\zeta_{\gamma} = 0. \quad (54)$$

If the set $\{\psi_s\}$ contains all the collision invariants, for example,

$$\psi_0 = 1, \quad \psi_i = \zeta_i, \quad \psi_4 = \zeta_i^2, \quad (55)$$

then each cubature point (term in (51)) ensures the conservation of mass, momentum and kinetic energy for the found *projective velocities* $\zeta_{\lambda_{\nu}+s_a}$ and *projection weights* $r_{\lambda_{\nu},a}$.

Second, to satisfy

$$J_{\gamma}(\hat{f}_{M\gamma}) = 0, \quad (56)$$

$\hat{f}_{\alpha'_{\nu}}$ is interpolated in the following way:

$$\frac{\hat{f}_{\alpha'_{\nu}}}{w_{\alpha'_{\nu}}} = \prod_{a \in \Lambda} \left(\frac{\hat{f}_{\lambda_{\nu}+s_a}}{w_{\lambda_{\nu}+s_a}} \right)^{r_{\lambda_{\nu},a}}. \quad (57)$$

This type of interpolation has a large computational cost, but is strictly required for low-noise analysis of slow flows, when the distribution function is close to the Maxwellian. In practice, the exponentiation can be performed with an error of about 10^{-5} , allowing several times to speed up the calculations. In addition, (57) ensures that the Boltzmann H-theorem holds in the discrete form [46]. For $\zeta_{\beta'_{\nu}}$ and $\hat{f}_{\beta'_{\nu}}$, all formulas are similar.

4.3 Solution of the Cauchy problem

Now turn to the space-homogeneous Boltzmann equation (47). Let f_{γ}^n denotes an approximate solution of (47) for velocity ζ_{γ} ($\gamma \in \Gamma$) at time t_n ($n \in \mathbb{N}$). Rewriting (51) as

$$\hat{J}_{\gamma}^n(\hat{f}_{\gamma}^n) = \sum_{\nu=1}^N \hat{\Delta}_{\gamma}^{n+(\nu-1)/N}(\hat{f}_{\gamma}^n), \quad N = |\mathcal{N}|, \quad (58)$$

where $\hat{\Delta}_\gamma^{n+(\nu-1)/N}$ is $\nu \in \mathcal{N}_n$ term of sum (51), one can apply the first-order explicit Euler method in fractional steps:

$$\hat{f}_\gamma^{n+\nu/N} = \hat{f}_\gamma^{n+(\nu-1)/N} + \tau \hat{\Delta}_\gamma^{n+(\nu-1)/N} \left(\hat{f}_\gamma^{n+(\nu-1)/N} \right), \quad (59)$$

where $\tau = t_{n+1} - t_n$ is the time step. Scheme (59) has a convergence rate $O(\tau|\Gamma|/|\mathcal{N}|)$ if all of the discrete velocities ζ_γ are distributed uniformly in the sequences $(\alpha_\nu)_{\nu=1}^N$ and $(\beta_\nu)_{\nu=1}^N$. This can be accomplished by a random permutation of the cubature sequence. For $|\Gamma|/|\mathcal{N}| = O(\tau)$, the second-order accuracy is achieved.

The Korobov lattice rule [47, 48] is used as an equal-weight cubature rule in (51). The integration lattice is randomly shifted every time step to obtain a sequence of sets of cubature points $(\mathcal{N}_n)_{n \in \mathbb{N}}$.

4.4 Preservation of positivity

Scheme (59) allows negative values of the distribution function and loses stability in the presence of them. To ensure its positivity, it is enough to require

$$\hat{f}_\gamma^{n+(j-1)/N} + \frac{\tau}{N} \hat{\Delta}_\gamma^{n+(j-1)/N} > 0 \quad (60)$$

for all $\gamma \in \Gamma$ and $\nu \in \mathcal{N}_n$. For $\gamma = \alpha_\nu$,

$$\hat{f}_{\alpha_\nu} - \frac{A}{N} \hat{f}_{\alpha_\nu} \hat{f}_{\beta_\nu} > 0, \quad A = \frac{\pi \tau V_\Gamma^2 N B_{\max}}{\sum_{\nu \in \mathcal{N}} w_{\alpha_\nu} w_{\beta_\nu}} \quad (61)$$

or

$$N > A \hat{f}_{\max}, \quad (62)$$

where

$$\hat{f}_{\max} = \max_{\gamma \in \Gamma} \hat{f}_\gamma, \quad B_{\max} = \max_{\substack{\gamma, \varsigma \in \Gamma \\ \omega \in S^2}} B(\omega, \zeta_\gamma, \zeta_\varsigma) = O(\zeta_{\max}), \quad \zeta_{\max} = \max_{\gamma \in \Gamma} |\zeta_\gamma|. \quad (63)$$

The same estimate holds for $\gamma = \beta_\nu$.

The projection nodes $\gamma = \lambda_\nu + s_a$ (and $\gamma = \mu_\nu + s_a$) are treated with interpolation (57). Additionally, assume $r_{\lambda_\nu, a} \leq 1$. For $r_{\lambda_\nu, a} \geq 0$,

$$N > A \hat{f}_{\max} \epsilon_f^2 \epsilon_w^2, \quad (64)$$

where

$$\epsilon_f = \max_{\substack{s_a, s_b \in \mathcal{S} \\ \gamma \in \Gamma}} \frac{\hat{f}_{\gamma+s_a}}{\hat{f}_{\gamma+s_b}}, \quad \epsilon_w = \max_{\gamma, \varsigma \in \Gamma} \frac{w_\gamma}{w_\varsigma}. \quad (65)$$

For a smooth distribution function, ϵ_f is proportional to the maximum *diameter* of the projection stencil

$$R_{\mathcal{S}} = \max_{\substack{s_a, s_b \in \mathcal{S} \\ \gamma \in \Gamma}} |\zeta_{\gamma+s_a} - \zeta_{\gamma+s_b}|. \quad (66)$$

For $r_{\lambda_\nu, a} < 0$,

$$\hat{f}_{\lambda_\nu+s_a} + \frac{A}{N} r_{\lambda_\nu, a} \hat{f}_{\alpha_\nu} \hat{f}_{\beta_\nu} > 0. \quad (67)$$

For an arbitrary distribution function, we obtain a very expensive estimate

$$N > A \hat{f}_{\max} \bar{r}_{\max} \max_{\gamma, \varsigma \in \Gamma} \frac{\hat{f}_\gamma}{\hat{f}_\varsigma}, \quad \bar{r}_{\max} = \max_{\gamma \in \Gamma, a \in \Lambda} (-r_{\gamma, a}), \quad (68)$$

but for a Maxwellian,

$$N > A \hat{f}_{\max} \epsilon_f^2 \bar{r}_{\max}. \quad (69)$$

In summary, to decrease N required for (60), one should construct a velocity grid that minimizes $|\Gamma|$, ζ_{\max} , ϵ_w and a projection stencil that minimizes R_S , \bar{r}_{\max} . ϵ_f can be lowered by means of grid refinement in regions of large gradients of the distribution function.

In practice, condition (60) for all ν requires a large computational cost. In order to achieve an acceptable accuracy, it is sufficient to exclude terms that violate (60) from (59). In other words, the collision integral can be calculated as

$$\hat{J}_\gamma^n = \sum_{\nu \in \mathcal{N} \setminus \mathcal{M}} \hat{\Delta}_\gamma^{n+(\nu-1)/N}, \quad (70)$$

where \mathcal{M} is the set of cubature points excluded from \mathcal{N} . To avoid a significant error in this integration method, it is necessary to control the contribution of excluded points to the collision integral. For example, N can be adjusted so that

$$\epsilon_J = \frac{\pi V_\Gamma^2}{\rho \sum_{\nu \in \mathcal{N}} w_{\alpha_\nu} w_{\beta_\nu}} \sum_{\nu \in \mathcal{M}} \left| \hat{f}_{\lambda_\nu} \hat{f}_{\mu_\nu} - \hat{f}_{\alpha_\nu} \hat{f}_{\beta_\nu} \right| B_\nu \quad (71)$$

appears to be sufficiently small. Interpolation (57) may lead to enormous values of $\hat{f}_{\alpha'_\nu}$ when one of $\hat{f}_{\lambda_\nu + s_a}$ is extremely small and the corresponding weight $r_{\lambda_\nu, a}$ is negative. For this reason, we avoid interpolation in (71).

4.5 Projection stencils

Hereinafter, the velocity grid is assumed to be rectangular in \mathbb{R}^3 ; therefore, it can be indexed by an integer vector, i.e., $\Gamma = \{\gamma : \gamma \in \mathbb{Z}^3\}$. A displacement rule can be also represented as an integer vector, i.e., $\mathcal{S} \subset \mathbb{Z}^3$. In this way, a sum of the indexes should be interpreted as a vector sum in \mathbb{Z}^3 . The projection method is second-order accurate with respect to the step of a rectangular velocity grid [49].

Due to the symmetry of a uniform grid, it is sufficient to use two projection nodes to ensure the conservative laws. In the general case, five projection nodes are necessary for the existence of a solution of (54) for (55). The diameter of the stencil R_S can be narrowed if seven projection nodes are employed. When $|\mathcal{S}| = n$, scheme (59) is called the n -point scheme.

The 2-point scheme is based on the symmetric projection

$$\delta_{\alpha'\gamma} = (1-r)\delta_{\lambda\gamma} + r\delta_{\lambda+s, \gamma}, \quad \delta_{\beta'\gamma} = (1-r)\delta_{\mu\gamma} + r\delta_{\mu-s, \gamma}, \quad (72)$$

where $\zeta_{\lambda+s} + \zeta_{\mu-s} = \zeta_\lambda + \zeta_\mu$ and

$$r = \frac{E_0 - E_1}{E_2 - E_1}, \quad E_0 = \zeta_{\alpha'}^2 + \zeta_{\beta'}^2, \quad E_1 = \zeta_\lambda^2 + \zeta_\mu^2, \quad E_2 = \zeta_{\lambda+s}^2 + \zeta_{\mu-s}^2. \quad (73)$$

Subindex ν is omitted for brevity. For this scheme, the following relations hold:

$$0 \leq r < 1, \quad h \leq R_S \leq \sqrt{3}h, \quad (74)$$

where $h^3 = w_\gamma = V_\Gamma/|\Gamma|$.

Let $\boldsymbol{\eta} = \zeta_{\alpha'} - \zeta_\lambda$, and \mathbf{h}_+ , \mathbf{h}_- be the minimal diagonal displacements from ζ_λ so that \mathbf{h}_+ is directed in the same octant as $\boldsymbol{\eta}$ and \mathbf{h}_- lies in the opposite one. Then, the compact 5-point scheme is constructed on the nodes

$$\zeta_{\lambda+s_0} = \zeta_\lambda, \quad \zeta_{\lambda+s_i} = \zeta_\lambda + (\mathbf{h}_+ \cdot \mathbf{e}_i)\mathbf{e}_i, \quad \zeta_{\lambda+s_4} = \zeta_\lambda + \mathbf{h}_-, \quad (75)$$

where \mathbf{e}_i is the basis of the rectangular velocity grid. The projection weights are

$$r_{\lambda,0} = 1 - \sum_{j=1}^4 r_{\lambda,j}, \quad r_{\lambda,i} = \frac{\eta_i - r_{\lambda,4}h_{-i}}{h_{+i}}, \quad r_{\lambda,4} = \frac{\boldsymbol{\eta} \cdot (\boldsymbol{\eta} - \mathbf{h}_+)}{\mathbf{h}_- \cdot (\mathbf{h}_- - \mathbf{h}_+)}. \quad (76)$$

For the uniform grid, the following relations hold:

$$0 < r_{\lambda,0} \leq 1, \quad -\frac{1}{12} \leq r_{\lambda,i} < \frac{11}{24}, \quad -\frac{1}{8} \leq r_{\lambda,4} \leq 0, \quad R_S = \sqrt{6}h. \quad (77)$$

The *symmetric 7-point scheme* is constructed on the nodes

$$\zeta_{\lambda+s_0} = \zeta_{\lambda}, \quad \zeta_{\lambda+s_{\pm i}} = \zeta_{\lambda} + (\mathbf{h}_{\pm} \cdot \mathbf{e}_i) \mathbf{e}_i. \quad (78)$$

The projection weights are

$$r_{\lambda,0} = 1 - \sum_{j=1}^3 r_{\lambda,j} + r_{\lambda,-j}, \quad r_{\lambda,\pm i} = \pm \frac{\eta_i(\eta_i - h_{\mp i})}{h_{\pm i}(h_{+i} - h_{-i})}. \quad (79)$$

There is no summation over repeated indices in (79). For the uniform grid, the following relations hold:

$$\frac{1}{4} \leq r_{\lambda,0} \leq 1, \quad 0 \leq r_{\lambda,\pm i} \leq \frac{3}{8}, \quad -\frac{1}{8} \leq r_{\lambda,\mp i} \leq 0, \quad R_S = 2h. \quad (80)$$

Both 5-point and 7-point schemes have $\bar{r}_{\max} = 1/8$. In order to reduce it, more projection nodes are required [33].

5 Numerical examples

In the present work, solver `snitSimpleFoam` [50], developed within the open-source computational platform OpenFOAM®, is employed for the KGF equations. The solver is extended to deal with the second-order boundary conditions. Grids are adjusted in such a way as to ensure the numerical error is less than 10^{-4} . The iterative process is stopped when the residual becomes less than 10^{-6} .

The described algorithm is implemented within the problem-solving environment for numerical analysis of rarefied gas flows [51, 52]. The physical grid is selected under the same criteria as for the numerical solution of the KGF equations, but needs additional exponential refinement near the diffuse-reflection boundaries to ensure the numerical error is less than 10^{-4} in the Knudsen layer. Both uniform and nonuniform velocity grids are used, while simulation on a detailed grid starts from a solution on a coarse grid to accelerate the steady-state convergence. For nonuniform grids, the symmetric 7-point scheme is employed, since it provides smaller ϵ_J for a smooth distribution function. The number of cubature points is adjusted so that $\epsilon_J < 10^{-5}$.

5.1 Flow between the parallel plates with the temperature distributed sinusoidally

Consider a plane periodic geometry, as shown in Fig. 1. Gas is placed between the two parallel plates at rest ($v_{Bi} = 0$) separated by unit distance. Their temperature is distributed sinusoidally:

$$T_B = 1 - \frac{\cos(2\pi x)}{2}. \quad (81)$$

The complete diffuse-reflection boundary condition is used at the plates. The gas density is normalized to unity, i.e.,

$$\int_0^1 \int_0^1 \rho dx dy = 1. \quad (82)$$

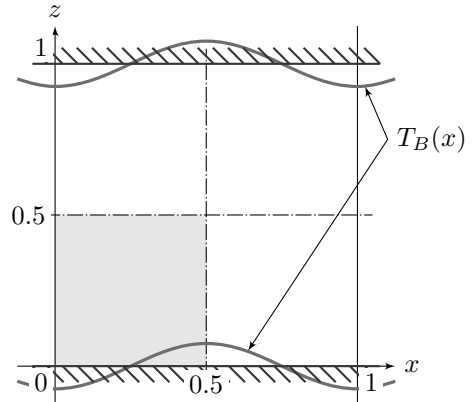


Figure 1: Geometry of the problem

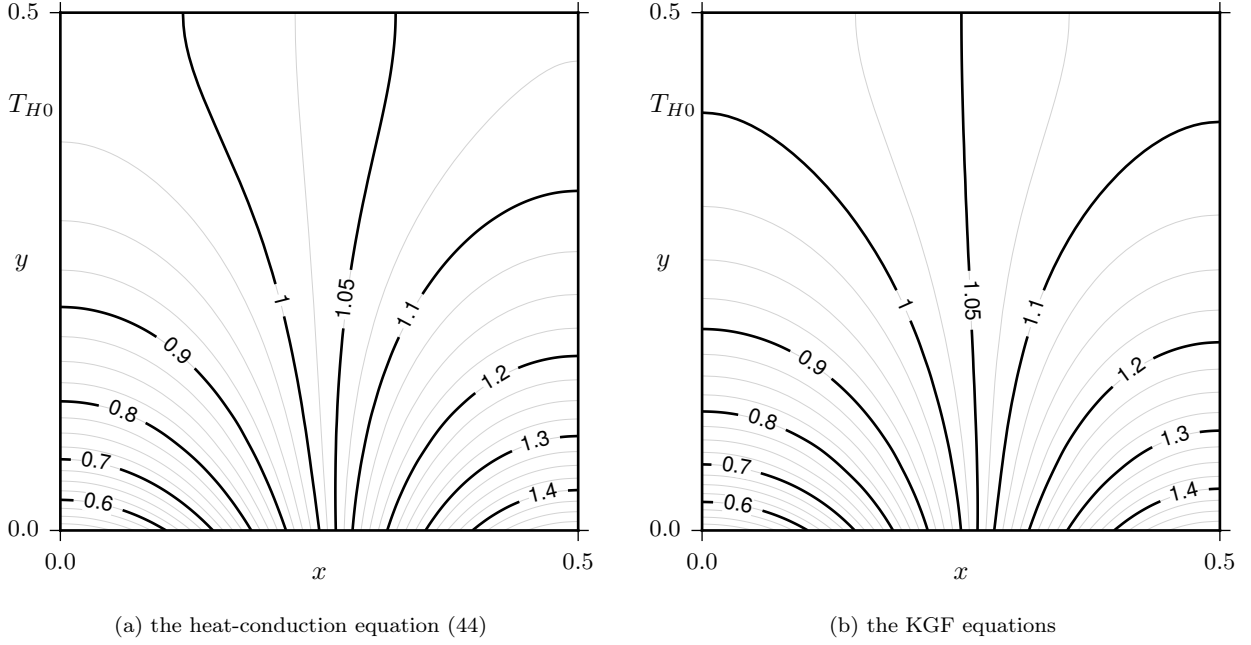


Figure 2: Isothermal lines in the continuum limit

Due to the symmetry of the problem, the computational domain is the square with the side $1/2$. It is grayed out in Fig. 1.

This problem was studied in [9] based both on the KGF equations and on the kinetic approach; however, only model Krook–Welanders equation was exploited due to the high complexity of the numerical approximation of the Boltzmann equation. For gas mixtures, some numerical results are presented in [53]. In the present paper, a direct solution of the Boltzmann equation is obtained for a hard-sphere gas. The asymptotic solution for small Kn is examined as part of the problem. In particular, a comparative analysis is performed for the high-order boundary conditions.

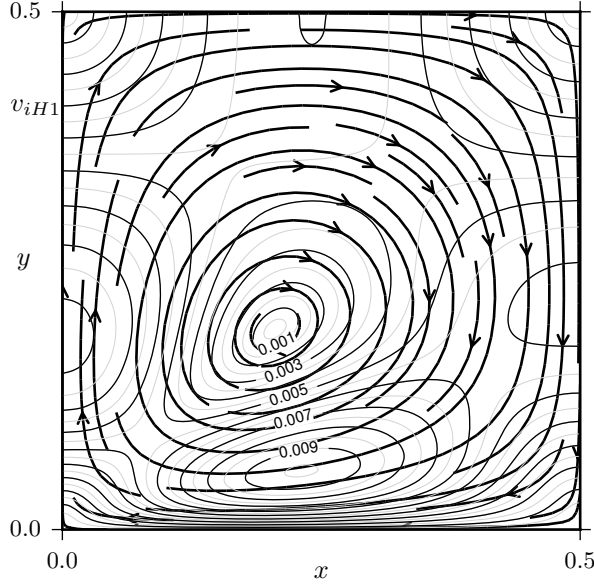
5.1.1 Solution in the continuum limit

For the numerical analysis of the problem, the rectangular grid is used in the physical space: the region $0 < x < 1/2$ is divided into 30 intervals of equal length, and the region $0 < y < 1/2$, into 40 intervals with refinement near $y = 0$.

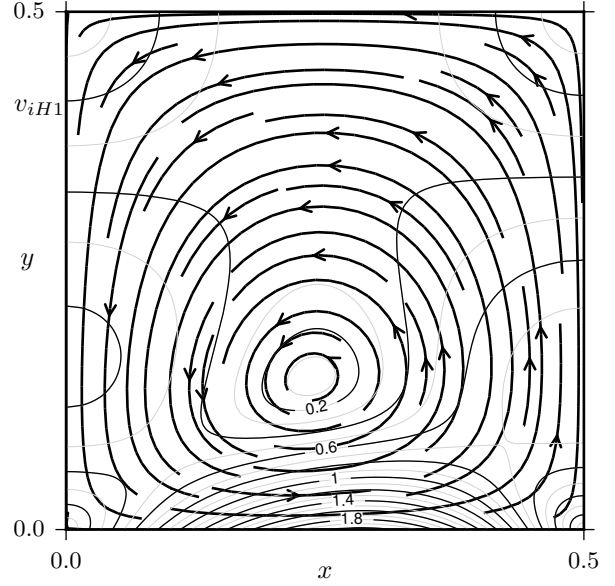
Fig. 2 shows the steady-state temperature field obtained as the solution of the heat-conduction and KGF equations. In the continuum limit, the heat-conduction equation is derived from the KGF equations, when $\bar{\gamma}_7 = 0$ and $K_1 = 0$. The thermal-creep flow is much stronger than the nonlinear thermal-stress one. This fact is demonstrated in Fig. 3, where the KGF equations are solved both with and without the thermal-creep boundary condition. Note also that direction of the gas flows are opposite in Fig. 3a and 3b. The results obtained in the continuum limit coincides with the presented in [9]. This fact can serve as a verification of the solver `snitSimpleFoam`.

5.1.2 Solution for arbitrary Knudsen numbers

To consider the problem in arbitrary range of Knudsen numbers, it is necessary to refer to the numerical solution of the Boltzmann equation. The physical grid is the same as in the solution of KGF equations;



(a) the KGF equations without thermal creep ($K_1 = 0$)

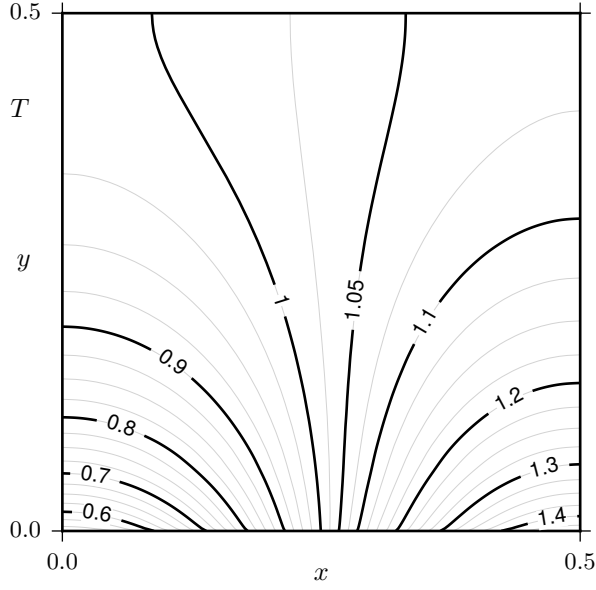


(b) the KGF equations

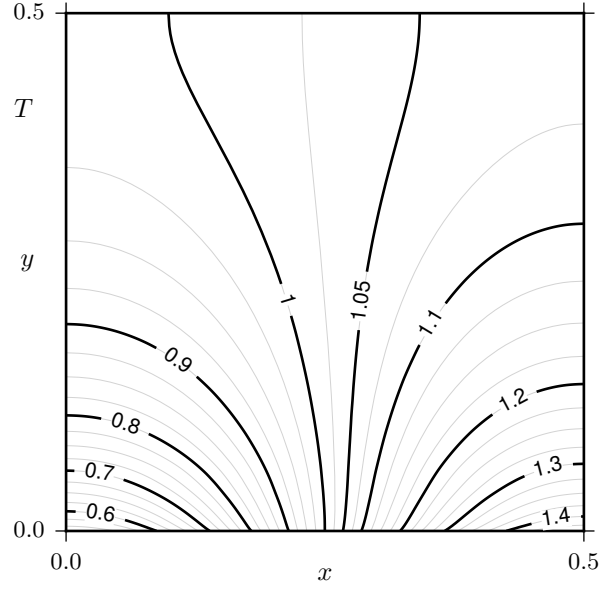
Figure 3: The velocity field v_{i1} in a continuum limit. Contour lines correspond to the magnitude, and curves with arrows show the direction.

Table 1: The parameters of the velocity grids: ζ_{cut} is the radius of the sphere that encloses all nodes, N_i is the maximum number of nodes along the x_i axis, $|\mathcal{V}|$ is the total number of nodes, $\min(\Delta\zeta_i)$ is the minimum distance between nodes along the x_i axis, $\delta T_M/T$ is the relative temperature error of the Maxwellian, $\delta T_{MM}/T$ is the relative temperature error of the sum of two half-Maxwellians, separated by the plane $\zeta_y = 0$

Grid	ζ_{cut}	$N_{x,z}/2$	$N_y/2$	$ \mathcal{V} $	$\min(\Delta\zeta_{x,z})$	$\min(\Delta\zeta_y)$	$\delta T_M/T$	$\delta T_{MM}/T$
M1	4.25	8	8	2176	0.53	0.53	$[-20, 0.3] \cdot 10^{-5}$	$[-4.0, 10] \cdot 10^{-5}$
M2	5.3	11	26	20248	0.4	0.005	$[2.3, 4.1] \cdot 10^{-5}$	$[2.7, 4.0] \cdot 10^{-5}$
M3	4.5	12	15	15568	0.05	0.005	$[4.0, 5.1] \cdot 10^{-3}$	$[4.4, 5.5] \cdot 10^{-3}$
M4	8.0	16	16	28640	0.1	0.1	$[1.65, 1.79] \cdot 10^{-3}$	$[3.1, 3.4] \cdot 10^{-3}$

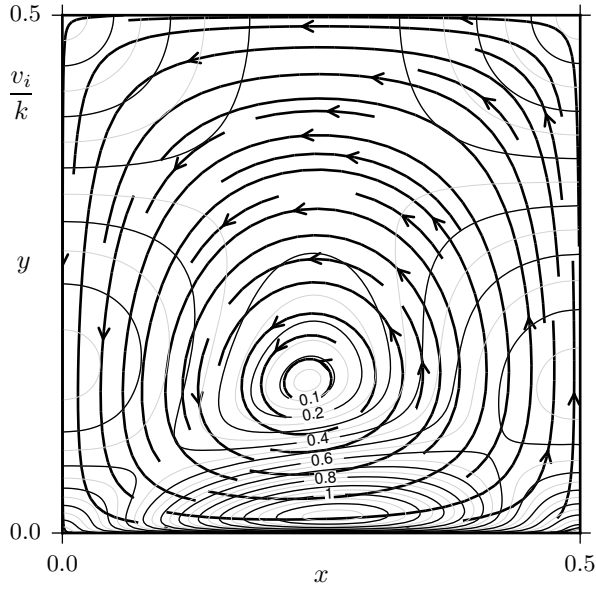


(a) The KGF equations with the second-order boundary conditions

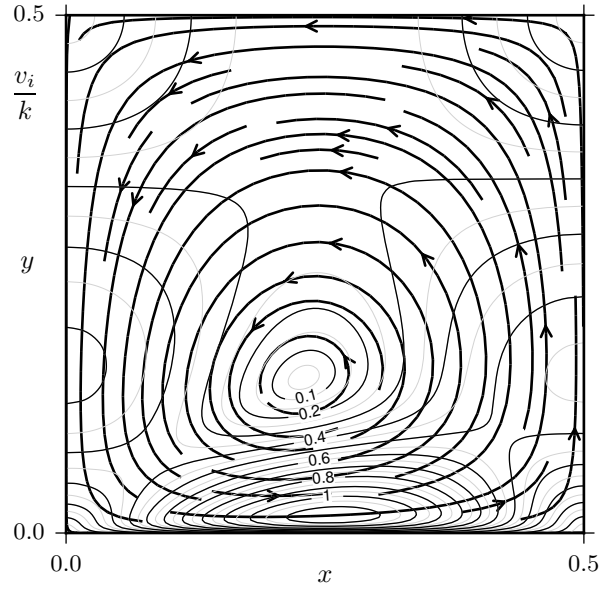


(b) the Boltzmann equation

Figure 4: Isothermal lines for $\text{Kn} = 0.01$



(a) the KGF equations with the second-order boundary conditions



(b) the Boltzmann equation

Figure 5: The velocity field for $\text{Kn} = 0.01$. Contour lines correspond to the magnitude, and curves with arrows show the direction.

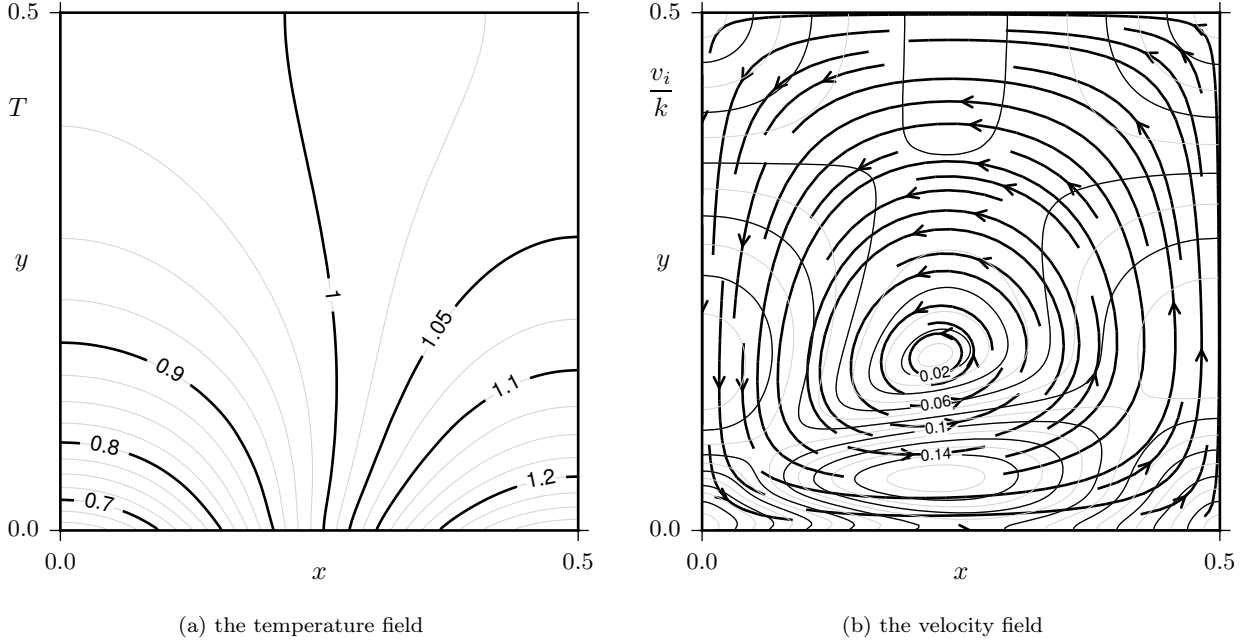


Figure 6: The solution of the Boltzmann equation for $\text{Kn} = 0.1$. Contour lines correspond to the magnitude, and curves with arrows show the direction.

however, it is additionally refined in the Knudsen layer (close to $y = 0$) so that the width of the boundary cell is equal to 0.02 mean free paths.

The numerical accuracy in the velocity space is controlled on several rectangular grids (M1, M2, M3), whose parameters are presented in Table 1. The problem is initially solved on the coarse uniform grid M1, and then the result is refined on the nonuniform grids. M2 nodes are arranged as the roots of the Hermite polynomial along the x and z axes, exponentially along the y axis. Such a strong refinement provides a careful approximation of the large variations of the distribution function in the Knudsen layer. The distance between M3 nodes grows quadratically along each axis. Unlike M2, M3 approximates cold distributions (a temperature close to $T = 0.5$) more accurately. Number of cubature points varies considerably: about 5×10^3 for M1 and about 5×10^4 for nonuniform grids. For very small Kn , the macroscopic fields are computed from time extrapolation instead of time averaging, since the achievement of the completely steady state (especially near $y = 1/2$) requires too many iterations of the explicit scheme.

For nonuniform grids, it is important to check the computational accuracy of the macroscopic variables (some cubatures of the form (48)). For example, the ranges of the relative temperature error for the Maxwellian (δT_M) and the sum of the two half-Maxwellians (δT_{MM}) are shown in Table 1. They are computed for the typical temperatures and velocities. Moments of a distribution function are calculated accurately on a coarse grid, if its nodes are arranged uniformly or as the roots of the Hermite polynomial. Otherwise, the velocity grid should be refined sufficiently as it is done along the y axis for M2. For M3, the temperature cubature (48) is always about 0.004 more than the true value and therefore can be adjusted in accordance with this value. For M1, the cubature error takes negative values for temperatures close to $T = 1.5$, because ζ_{cut} is not sufficiently large.

Fig. 4 and 5 show the temperature and velocity fields for $\text{Kn} = 0.01$. The numerical solutions of the Boltzmann and KGF equations can be compared for small Kn . It is clearly seen that the temperature field obtained with the high-order boundary conditions (Fig. 4a) significantly better approximates the exact solution (Fig. 4b) compared with the solution obtained with the leading-order ones (Fig. 2b).

Fig. 6 represents the solution for $\text{Kn} = 0.1$. With the increase in Kn , the thermal-creep flow and

temperature jump near the boundary $y = 0$ amplify. The point of maximum gas velocity moves away from the plate.

To demonstrate the convergence of the Boltzmann solution to the KGF one in a continuum limit, some boundary integrals versus the Knudsen number are presented in Fig. 7. It is seen from Fig. 7a that all boundary conditions for the KGF equations, together with the corresponding Knudsen-layer corrections, approximate the numerical solution of the Boltzmann equation with the stated accuracy. In particular, the condition (25) yields the error $O(k)$, the first-order temperature jump leads to $O(k^2)$, and the second-order jump improves the convergence up to $O(k^3)$. Note that the solution obtained on the coarse uniform grid M1 is almost identical to the M2 solution and to the adjusted M3 one.

In Fig. 7b, the same convergence rates are observed for v_i . Since v_i/k is depicted, the error of the numerical solution of the Boltzmann solution increased for small k . The M2 and M3 solutions are almost identical, but differ by a constant value (about 0.008) from the M1 solution. Thus, discontinuities, as well as their decay in the Knudsen layer, of the distribution function on the diffuse-reflection boundary make a negligible contribution to the overall solution. For slow flows, it is explained by the fact that these discontinuities are $O(k)$. This observation allows us to consider the distribution function is smooth enough without significant loss in accuracy; therefore, it is possible to avoid adaptation of the velocity grid to the geometry of the problem.

The fluid-dynamic and kinetic solutions differ, as expected, on the magnitude $O(k)$ away from the diffuse-reflection boundary. It is demonstrated in Fig. 7c and 7d. It is clearly seen from Fig. 7c that the solution of the Boltzmann equation converges to the solution of the KGF equations rather than the heat-conduction equation. The corrected M3 solution is almost identical with M2 and slightly exceeds M1 (about 0.001). This difference seems to be explained by a rough approximation of the M1 grid. It is also seen from Fig. 7c and 7d that the second-order boundary conditions have little effect on the solution of KGF equations; however, the accuracy of the asymptotic solution is significantly improved if only the temperature and velocity jumps are included in the boundary conditions.

5.2 Flow between two uniformly heated elliptic cylinders

Consider a gas between two uniformly heated coaxial elliptical cylinders arranged so that its large axes are rotated through the angle $\beta = \pi/2$. a_0 and b_0 are semi-axes of the inner cylinder, T_0 is its temperature, a_1 and b_1 are semi-axes of the outer cylinder, T_1 is its temperature. Numerical analysis of the steady-state problem for

$$a_0 = 0.3, \quad b_0 = 0.7, \quad T_0 = 1, \quad a_1 = 1.5, \quad b_1 = 1, \quad T_1 = 5$$

is available in the literature. In particular, a statistical simulation (DSMC) for $0.1 \leq \text{Kn} \leq 5$ is presented in [54], the moment of the forces acting on the cylinder depending on the rotation angle β is studied on the basis of KGF equations in [50].

In the present study, the numerical solution of the Boltzmann equation for the hard-sphere model is compared with the asymptotic solution based on the KGF equations and boundary conditions of different order. Due to the symmetry of the problem, consider only the first quadrant ($x > 0, y > 0$), assuming that the common axis of the cylinders is located in the origin of coordinates. There are several types of flows depending on the Knudsen number. In the continuum limit, the nonlinear thermal-stress flow occupies the entire volume and is directed counterclockwise [11, 50]. For $\text{Kn} > 0.1$, on the contrary, the clockwise flow dominates, while the nonlinear thermal-stress flow occupies only small region most remote from the inner cylinder [54]. The strong near-boundary clockwise flow is driven by the tangential gradient of the gas temperature. For $\text{Kn} < 0.1$, the dependence of the flow regime on the Knudsen number has not been studied in the literature. The competition pattern between the first- and second-order nonlinear thermal-stress flows has also not been obtained until now. In particular, it requires a huge computational effort to achieve an acceptable signal-to-noise ratio and discern the structure of these flows by the DSMC method.

For $\text{Kn} = 0.02$, the structured physical mesh consists of $N_V = 2401$ of quadrilateral cells, which is constructed by the transfinite interpolation method implemented in the GMSH package [55]. The longitudinal cell edges are nearly tangent to the isothermal surfaces, and the transverse cell edges to the temperature

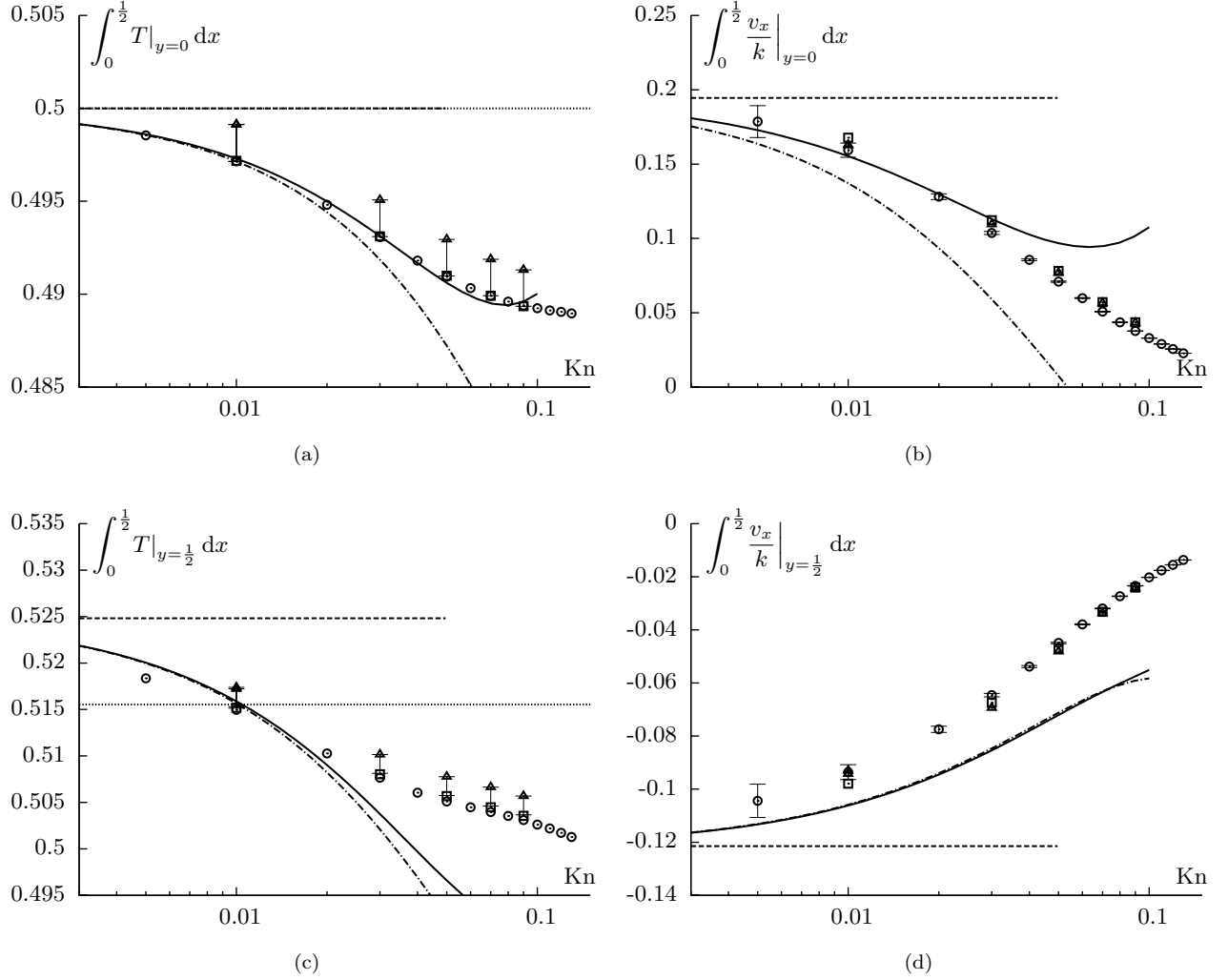
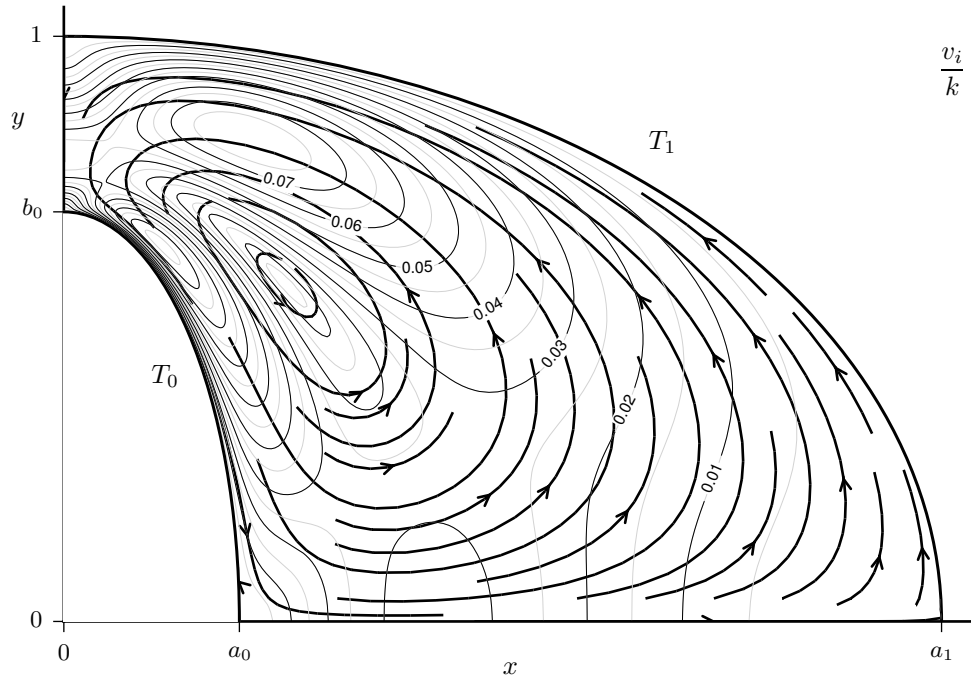
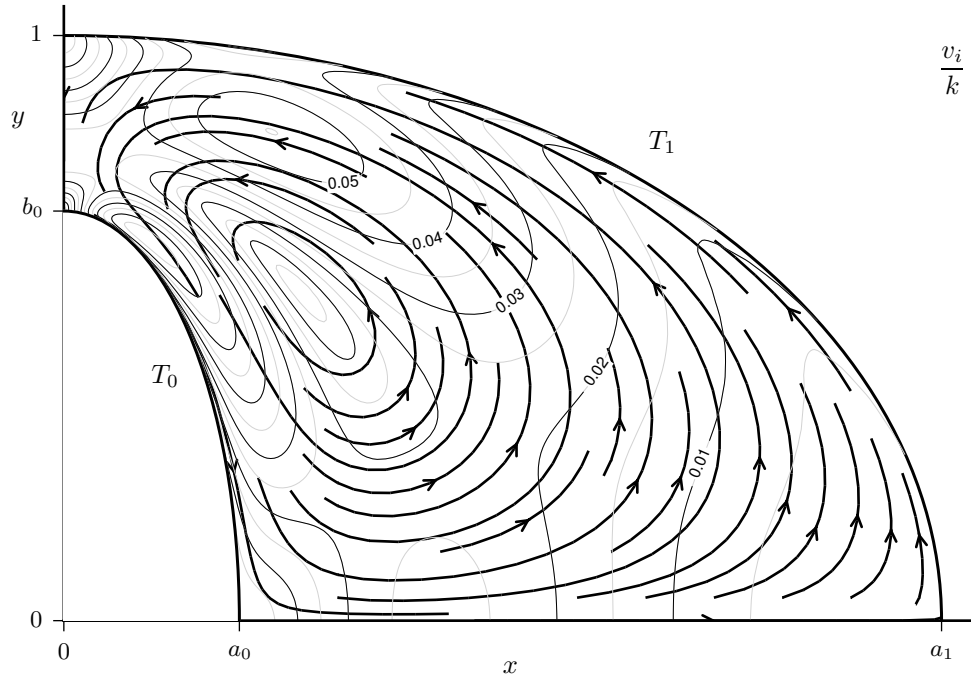


Figure 7: Some boundary integrals, obtained by different methods: the heat-conduction equation $\cdots\cdots$, the KGF equations with the leading-order (only thermal creep) $---$, first-order $-\cdots-$, and second-order $---$ boundary conditions, the Boltzmann equation on grids M1 \circ , M2 \square , and M3 \triangle . Error bars for M3 correspond to the temperature correction in accordance with the cubature error for a Maxwellian. Error bars for M1 correspond to the relative error 3×10^{-4} .

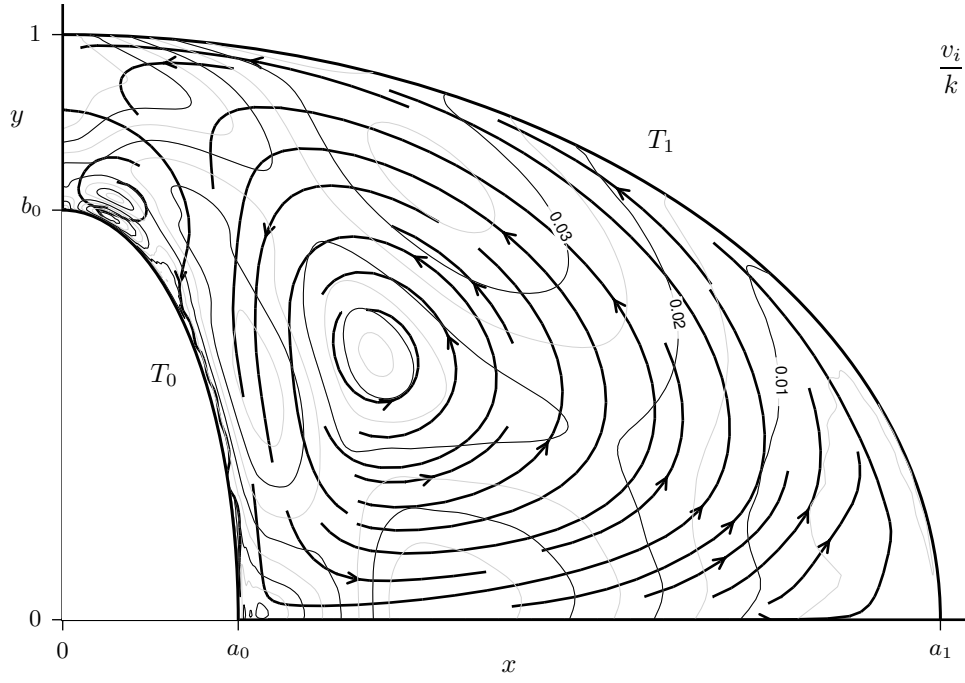


(a) the KGF equations with the leading-order boundary conditions



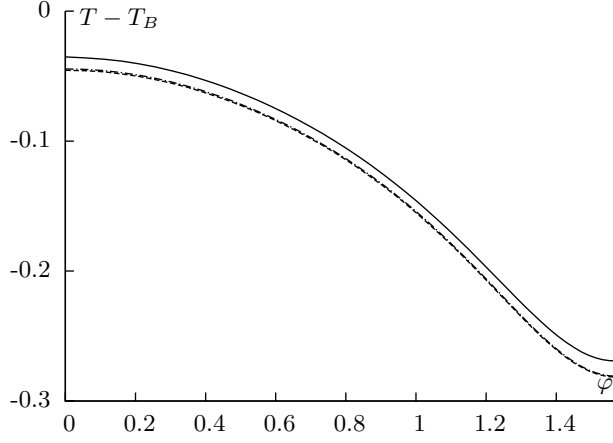
(b) the KGF equations with the second-order boundary conditions

Figure 8: The velocity field for $\text{Kn} = 0.02$. Contour lines correspond to the magnitude, and curves with arrows show the direction.

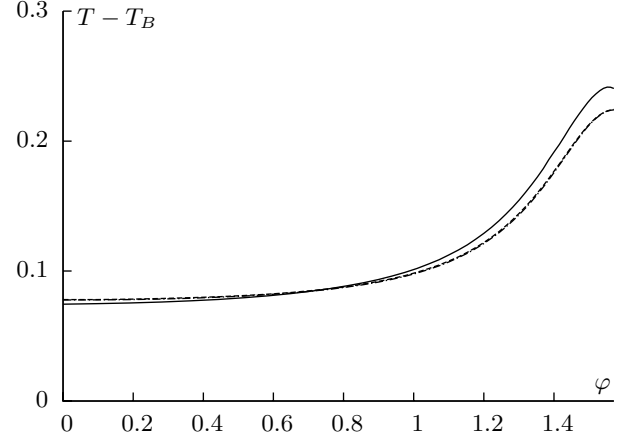


(c) the Boltzmann equation

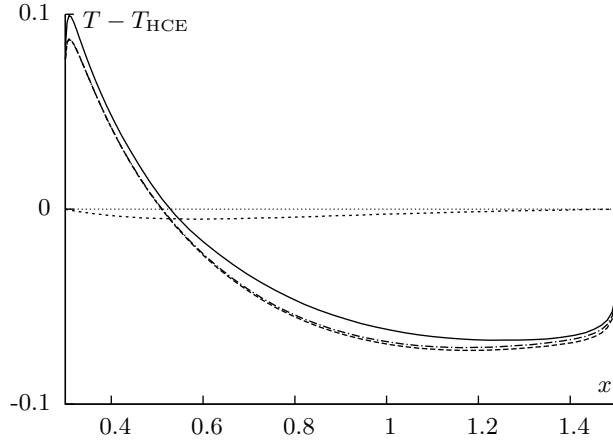
Figure 8: (cont.) The velocity field for $\text{Kn} = 0.02$. Contour lines correspond to the magnitude, and curves with arrows show the direction.



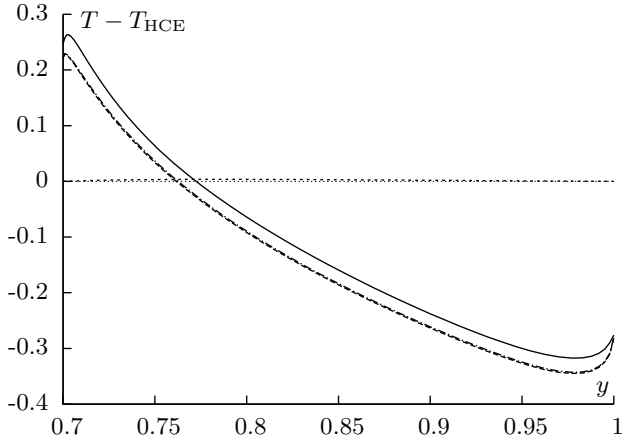
(a) the outer ellipse



(b) the inner ellipse



(c) the semi-major axis of the outer cylinder



(d) the semi-minor axis of the outer cylinder

Figure 9: The profile of the boundary temperature. The angle φ corresponds to the polar coordinates $x = r \cos \varphi$, $y = r \sin \varphi$. T_{HCE} is the temperature field, described by the heat-conduction equation. The following solutions are presented: the Boltzmann equation — (divided by 1.0017), the KGF equations with the leading-order $\cdots\cdots$, first-order $---$, and second-order $- \cdots -$ boundary conditions.

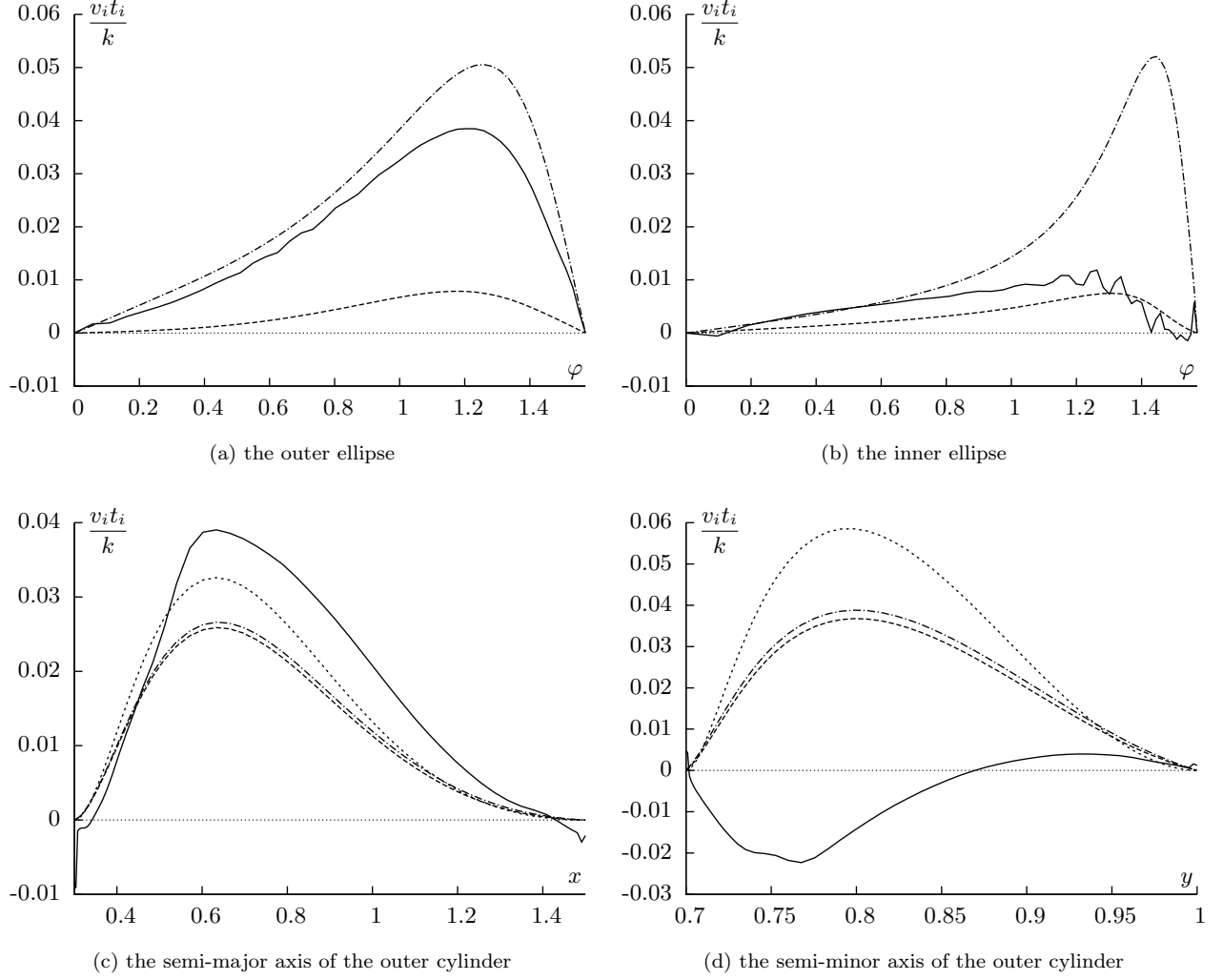


Figure 10: The profile of the boundary tangential velocity. The angle φ corresponds to the polar coordinates $x = r \cos \varphi$, $y = r \sin \varphi$. Unit vector t_i is directed counterclockwise. The following solutions are presented: the Boltzmann equation —, the KGF equations with the leading-order \cdots , first-order $---$, and second-order $- \cdots -$ boundary conditions.

gradient. Near the cylindrical surfaces, especially in the region of large temperature gradient, the physical mesh is refined so that the minimum width of the cell is equal to 0.046 mean free paths. The symmetric nonuniform grid M4 (see Table 1) is constructed in the velocity space. The distance between nodes increases quadratically along each axis. This velocity grid provides a sufficiently accurate approximation of the distribution function for a wide temperature range from T_0 to T_1 .

It takes about 10^5 iterations with 5×10^4 cubature points to reach the steady state of the numerical solution of the Boltzmann equation, if the initial distribution is determined from the asymptotic solution. This computation lasts several days on a personal computer with CPU 4×3 GHz. The steady-state time averaging helps to reduce a statistical noise arising from the random shifting of the cyclic Korobov lattice.

The velocity field obtained by different methods is shown in Fig. 8. The second-order boundary conditions (Fig. 8b) does not change the qualitative picture of the flow in comparison with the leading-order ones, but only weaken the whole flow due to the velocity jump and second-order thermal slip. The numerical solution of the Boltzmann equation, however, shows a different flow pattern, where another clockwise flow competes against the counterclockwise nonlinear thermal-stress one. This flow occurs in the region where the temperature gradient and curvature of the boundary surface reach their maximum but outside of the Knudsen layer; therefore, it cannot be described directly through boundary conditions. Indeed, $u_{iH1} = 0$ on the boundary, because $t_i \partial T_{H0} / \partial x_i = 0$ (t_i is a unit vector tangent to the boundary). The second-order thermal-stress slip is counterclockwise ($a_4 > 0$), but is balanced by the third-order terms associated with the curvature, proportional to $\kappa t_i \partial T_{H1} / \partial x_i$ (κ is the curvature of the boundary surface). In other words, $u_{iH2} t_i$ and $u_{iH3} t_i$ have opposite signs. Numerical analysis with the nonlinear second-order boundary conditions has not been carried out, since the coefficient in front of $(t_i \partial T_{H1} / \partial x_i)(n_j \partial T_{H0} / \partial x_j)$ is unknown.

As can be seen from Fig. 8, the leading-order asymptotic solution incorrectly describes the velocity field even for $\text{Kn} = 0.02$. Indeed, the considered boundary-value problem leads to the region, where the temperature gradient is comparable with the inverse Knudsen number, which means $kn_i \partial f / \partial x_i = O(f)$, but in contrast to the Knudsen layer, the temperature gradient decreases slowly. In this region, strictly speaking, the asymptotic solution in the form (7) cannot be found; however, it seems the correct flow pattern can be obtained by the use of the next-order (hitherto unknown) equations for T_{H1} , u_{iH2} , p_{H3} . In this case, the next-order part of the asymptotic solution is comparable to the leading-order one.

Before proceeding to analysis of the boundary profiles, specify the method of calculating the temperature on a diffuse-reflection surface. Actually, the finite-volume solution provides solution only in the cell centers. Since the temperature has a weak logarithmic singularity in the Knudsen layer, the boundary temperature is extrapolated as $Ay \ln y + B$, where A and B are constants, y is the distance from the boundary. In the previous problem, it was sufficient to use the linear extrapolation, because the width of the boundary cell and normal temperature gradient were less.

Fig. 9 and 10 show the temperature and velocity profiles on the boundary surfaces. The inclusion of the first-order temperature jump in the boundary conditions yields a significant improvement to the asymptotic temperature field, while the second-order temperature jump gives only a small correction. This is due to the fact that $n_i \partial T_{H0} / \partial x_i$ and $n_i n_j \partial^2 T_{H0} / \partial x_i \partial x_j$ are comparable but much larger than T_{H0} . In Fig. 9, due to the cubature error for temperature, the numerical solution exceeds the asymptotic one less than 0.004; however, in Fig. 9d and for $\varphi > \pi/3$ in Fig. 9b, the difference between the solutions is larger due to the considerable discrepancy between the velocity fields u_i/k , affecting the temperature field through the energy equation (12). Indeed, Fig. 10d shows that the corresponding values of $(u_i/kT) \partial T / \partial x_i$ differ even in sign.

The second-order boundary conditions provide a better approximation of the numerical solution at the outer cylinder (Fig. 10a), but do not at the inner one (Fig. 10b). As mentioned above, this is due to the fact that the boundary conditions for u_{iH3} are $O(u_{iH2}/k)$ in the region of maximum temperature gradient, but are not included in the solution of the KGF equations. Sharp fluctuations in the numerical solution of the Boltzmann equation (especially in Fig. 10b) come from the discretization error in the velocity space, but do not exceed 10^{-4} in absolute value of u_i .

6 Conclusion

Some numerical examples of slow nonisothermal slightly rarefied gas flows, as well as their influence on the temperature field, have been analyzed. With the help of the Tcheremissine's projection-interpolation discrete-velocity method, the flow patterns have been obtained with an accuracy that is unattainable by the conventional DSMC method. Adjusting the discretization of the velocity space is the main difficulty for nonlinear problems, including flows driven by large temperature variations. In the present work, this problem has been handled by using nonuniform velocity grids, which, however, complicates the calculations. In particular, the conservative projection onto a nonuniform grid requires a more complex algorithm and more cubature points. In addition, the cubature error for distributions that are close to the Maxwellian, typical for slow flows, grows significantly. Nevertheless, for small Knudsen numbers, the obtained numerical solutions coincide with the asymptotic ones with high accuracy. Hence, projection-interpolation method on nonuniform grids can be recommended for simulation a wide range of slow nonisothermal gas flows.

Upon comparative analysis of the numerical and asymptotic solutions of the Boltzmann equation for a hard-sphere gas, the Kogan–Galkin–Fridlander equations with appropriate boundary conditions have been shown to correctly describe slow nonisothermal gas flows for sufficiently small Knudsen numbers. If there is a temperature variation comparable to unity on the scale of the mean free path, then the fluid-dynamic approach is inapplicable to describe the rarefied gas. Instead, the problem should be discussed within the framework of the Boltzmann equation.

The boundary conditions that comprise the first-order temperature and velocity jumps along with the leading-order thermal creep have been shown to significantly improve the accuracy of an asymptotic solution, since large normal temperature gradients are typical for the considered problems. Including the next-order terms in the boundary conditions for the KGF equations gives a small correction and hence can be recommended only for high-accuracy numerical analysis.

The slip/jump coefficients in the boundary conditions, together with the Knudsen-layer functions, are obtained from the numerical solutions of the corresponding one-dimensional linearized problems. Currently, they are known only for the hard-sphere molecular potential and some model equations [56]. This fact limits the use in applied problems. Furthermore, the corresponding second-order Knudsen-layer problems for the nonlinear boundary-condition terms, which are reduced to the inhomogeneous linearized Boltzmann equation, are not analyzed even for a hard-sphere gas.

Acknowledgement

The author is grateful to Oscar Fridlander for fruitful discussions, which served as the starting point to the present study, to Vladlen Galkin for his detailed and valuable comments that helped to improve the presentation of the material, and to Felix Tcheremissine for his encouragement and interest in this work.

References

- [1] V. S. Galkin, M. N. Kogan, O. G. Fridlender, Some kinetic effects in continuum flows, *Fluid Dyn.* 5 (3) (1970) 364–371. doi:10.1007/BF01019269.
- [2] V. S. Galkin, M. N. Kogan, O. G. Fridlender, Free convection in a gas in the absence of external forces, *Fluid Dyn.* 6 (3) (1971) 448–457. doi:10.1007/BF01013999.
- [3] V. S. Galkin, O. G. Fridlender, On forces due to barnett stresses acting on bodies in a gas, *J. Appl. Math. Mech.* 38 (2) (1974) 244–257. doi:10.1016/0021-8928(74)90064-1.
- [4] V. S. Galkin, Derivation of the equations of slow gas mixture flows from the boltzmann equations, *Uch. Zap. TsAGI* 5 (4) (1974) 40–47, in russian.

- [5] M. N. Kogan, V. S. Galkin, O. G. Fridlender, Stresses produced in gases by temperature and concentration inhomogeneities. new types of free convection, *Phys. Usp.* 19 (5) (1976) 420–428. doi: 10.1070/PU1976v019n05ABEH005261.
- [6] V. S. Galkin, S. V. Rusakov, The gas dynamics equations of slow flows of polyatomic gas mixtures, non-uniform in temperature and concentrations, *J. Appl. Math. Mech.* 79 (2) (2015) 148–158. doi: 10.1016/j.jappmathmech.2015.07.005.
- [7] D. Burnett, The distribution of velocities in a slightly non-uniform gas, *P. London Math. Soc.* 2 (1) (1935) 385–430. doi:10.1112/plms/s2-39.1.385.
- [8] S. Chapman, T. G. Cowling, The mathematical theory of non-uniform gases: an account of the kinetic theory of viscosity, thermal conduction and diffusion in gases, Cambridge University Press, Cambridge, 1960.
- [9] Y. Sone, K. Aoki, S. Takata, H. Sugimoto, A. V. Bobylev, Inappropriateness of the heat-conduction equation for description of a temperature field of a stationary gas in the continuum limit: Examination by asymptotic analysis and numerical computation of the Boltzmann equation, *Phys. Fluids* 8 (1996) 628. doi:10.1063/1.868846.
- [10] Y. Sone, Kinetic theory and fluid dynamics, Birkhäuser, Boston, 2002.
- [11] Y. Sone, Molecular gas dynamics: theory, techniques, and applications, Birkhäuser, Boston, 2007.
- [12] A. V. Zhibakova, O. G. Fridlender, Heat transfer in slow gas flows, *Uch. Zap. TsAGI* 9 (5) (1978) 125–128, in russian.
- [13] V. Alexandrov, A. Boris, O. Friedlander, M. Kogan, Yu. Nikolsky, V. Perminov, Thermal stress effect and its experimental detection, in: C. Shen (Ed.), *Rarefied Gas Dynamics*, Peking University Press, Beijing, China, 1997, Ch. Rarefied Flow Studies, pp. 79–84.
- [14] V. Yu. Alexandrov, O. G. Friedlander, Yu. V. Nikolsky, Numerical and experimental investigations of thermal stress effect on nonlinear thermomolecular pressure difference, in: A. D. Ketsdever, E. P. Muntz (Eds.), *Rarefied Gas Dynamics*, AIP, New York, 2003, Ch. Rarefied Flow Studies, pp. 250–257.
- [15] V. Yu. Aleksandrov, Numerical analysis of the influence of thermal stresses on the nonlinear thermomolecular pressure difference effect, *Fluid Dyn.* 37 (6) (2002) 983–995. doi:10.1023/A:1022316817066.
- [16] C.-J. T. Laneryd, K. Aoki, P. Degond, L. Mieussens, Thermal creep of a slightly rarefied gas through a channel with curved boundary, in: M. S. Ivanov, A. K. Rebrov (Eds.), *Rarefied Gas Dynamics*, Siberian Branch of the Russian Academy of Sciences, Novosibirsk, 2007, pp. 1111–1116.
- [17] V. Yu. Aleksandrov, O. G. Fridlender, Slow gas motions and the negative drag of a strongly heated spherical particle, *Fluid Dyn.* 43 (3) (2008) 485–492. doi:10.1134/S0015462808030162.
- [18] V. Yu. Aleksandrov, Drag of a strongly heated sphere at small Reynolds numbers, *Fluid Dyn.* 46 (5) (2011) 794–808. doi:10.1134/S0015462811050139.
- [19] I. N. Larina, V. A. Rykov, Kinetic model of the boltzmann equation with limiting gas flow regimes at low knudsen numbers, *Comput. Math. Math. Phys.* 48 (7) (2008) 1221–1233. doi:10.1134/S0965542510120134.
- [20] V. Yu. Aleksandrov, A. I. Erofeev, M. N. Kogan, O. G. Friedlander, Temperature force of interaction between spherical particles, *Fluid Dyn.* 43 (2) (2008) 327–331. doi:10.1134/S001546280802018X.
- [21] C.-J. T. Laneryd, K. Aoki, S. Takata, Slow flows of a vapor-gas mixture with large density and temperature variations in the near-continuum regime, *Phys. Fluids* 19 (2007) 107104. doi:10.1063/1.2796213.

- [22] S. Rjasanow, W. Wagner, Stochastic numerics for the Boltzmann equation, Springer, 2005. doi:10.1007/3-540-27689-0.
- [23] G. A. Radtke, J.-P. M. Péraud, N. G. Hadjiconstantinou, On efficient simulations of multiscale kinetic transport, Philos. Trans. A Math. Phys. Eng. Sci. 371 (1982) (2013) 20120182. doi:10.1098/rsta.2012.0182.
- [24] G. Dimarco, L. Pareschi, Numerical methods for kinetic equations, Acta Numer. 23 (2014) 369–520. doi:10.1017/S0962492914000063.
- [25] L. Mieussens, A survey of deterministic solvers for rarefied flows, AIP Conf. Proc. 1628 (2014) 943–951. doi:10.1063/1.4902695.
- [26] M. Hattori, S. Takata, Second-order Knudsen-layer analysis for the generalized slip-flow theory I, Bull. Inst. Math. Acad. Sinica 10 (2015) 423–448.
- [27] M. Hattori, S. Takata, Second-order Knudsen-layer analysis for the generalized slip-flow theory II: curvature effects, J. Stat. Phys. 161 (4) (2015) 1010–1036. doi:10.1007/s10955-015-1364-0.
- [28] F. G. Cheremisin, Conservative method of calculating the Boltzmann collision integral, Phys. Dokl. 43 (1997) 607–610.
- [29] F. G. Cheremisin, Solving the Boltzmann equation in the case of passing to the hydrodynamic flow regime, Dokl. Phys. 45 (8) (2000) 401–404. doi:10.1134/1.1310733.
- [30] F. G. Tcheremissine, Conservative evaluation of Boltzmann collision integral in discrete ordinates approximation, Comput. Math. with Appl. 35 (1) (1998) 215–221. doi:10.1016/s0898-1221(97)00269-1.
- [31] F. G. Tcheremissine, Solution to the Boltzmann kinetic equation for high-speed flows, Comp. Math. Math. Phys. 46 (2) (2006) 315–329. doi:10.1134/S0965542506020138.
- [32] O. Rogozin, Numerical analysis of the nonlinear plane Couette-flow problem of a rarefied gas for hard-sphere molecules, Eur. J. Mech. B/Fluids 60 (2016) 148–163. doi:10.1016/j.euromechflu.2016.06.011.
- [33] O. I. Dodulad, F. G. Tcheremissine, Multipoint conservative projection method for computing the Boltzmann collision integral for gas mixtures, AIP Conf. Proc. 1501 (2012) 302–309. doi:10.1063/1.4769529.
- [34] A. V. Bobylev, Quasistationary hydrodynamics for the Boltzmann equation, J. Stat. Phys. 80 (5-6) (1995) 1063–1083. doi:10.1007/BF02179864.
- [35] C. D. Levermore, W. Sun, K. Trivisa, A low Mach number limit of a dispersive Navier–Stokes system, SIAM J. Math. Anal. 44 (3) (2012) 1760–1807. doi:10.1137/100818765.
- [36] W. Tan, Blow up criterion for the 3D ghost effect system, Nonlinear Anal. Real 29 (2016) 58–67. doi:10.1016/j.nonrwa.2015.10.008.
- [37] N. B. Maslova, Kramers problem in the kinetic theory of gases, USSR Comp. Math. Math. Phys. 22 (3) (1982) 208–219. doi:10.1016/0041-5553(82)90141-0.
- [38] C. Bardos, R. E. Caflisch, B. Nicolaenko, The Milne and Kramers problems for the Boltzmann equation of a hard sphere gas, Comm. Pure Appl. Math. 39 (3) (1986) 323–352. doi:10.1002/cpa.3160390304.
- [39] T. Ohwada, Y. Sone, K. Aoki, Numerical analysis of the shear and thermal creep flows of a rarefied gas over a plane wall on the basis of the linearized Boltzmann equation for hard-sphere molecules, Phys. Fluids A 1 (9) (1989) 1588–1599. doi:10.1063/1.857304.

- [40] Y. Sone, T. Ohwada, K. Aoki, Temperature jump and Knudsen layer in a rarefied gas over a plane wall: Numerical analysis of the linearized Boltzmann equation for hard-sphere molecules, *Phys. Fluids A* 1 (2) (1989) 363–370. doi:10.1063/1.857457.
- [41] S. Takata, M. Hattori, Numerical data for the generalized slip-flow theory, <http://hdl.handle.net/2433/199811> (2015).
- [42] T. Ohwada, Y. Sone, Analysis of thermal stress slip flow and negative thermophoresis using the Boltzmann equation for hard-sphere molecules, *Eur. J. Mech. B/Fluids* 11 (1992) 389–414.
- [43] P. L. Bhatnagar, E. P. Gross, M. Krook, A model for collision processes in gases. i. small amplitude processes in charged and neutral one-component systems, *Phys. Rev.* 94 (1954) 511–525. doi:10.1103/PhysRev.94.511.
- [44] P. Welander, On the temperature jump in a rarefied gas, *Ark. Fys.* 7 (1954) 507–553.
- [45] Y. Sone, K. Yamamoto, Flow of rarefied gas over plane wall, *J. Phys. Soc. Japan* 29 (2) (1970) 495–508. doi:10.1143/JPSJ.29.495.
- [46] O. I. Dodulad, F. G. Tcheremissine, Computation of a shock wave structure in monatomic gas with accuracy control, *Comp. Math. Math. Phys.* 53 (6) (2013) 827–844. doi:10.1134/S0965542513060055.
- [47] N. M. Korobov, The approximate computation of multiple integrals, *Dokl. Akad. Nauk SSSR* 124 (6) (1959) 1207–1210.
- [48] I. H. Sloan, S. Joe, *Lattice methods for multiple integration*, Oxford University Press, 1994.
- [49] Yu. A. Anikin, On the accuracy of the projection computation of the collision integral, *Comp. Math. Math. Phys.* 52 (4) (2012) 697–719. doi:10.1134/S0965542512040021.
- [50] O. A. Rogozin, Computer simulation of slightly rarefied gas flows driven by significant temperature variations and their continuum limit, *Theor. Comput. Fluid Dyn.* 28 (6) (2014) 573–587. doi:10.1007/s00162-014-0334-5.
- [51] Yu. A. Anikin, E. P. Derbakova, O. I. Dodulad, Yu. Yu. Kloss, D. V. Martynov, O. A. Rogozin, P. V. Shuvalov, F. G. Tcheremissine, Computing of gas flows in micro- and nanoscale channels on the base of the Boltzmann kinetic equation, *Procedia Comput. Sci.* 1 (1) (2010) 735–744. doi:10.1016/j.procs.2010.04.079.
- [52] Yu. A. Anikin, O. Dodulad, Yu. Yu. Kloss, D. Martynov, P. Shuvalov, F. Tcheremissine, Development of applied software for analysis of gas flows in vacuum devices, *Vacuum* 86 (11) (2012) 1770–1777. doi:10.1016/j.vacuum.2012.02.024.
- [53] L. Wu, J. Zhang, J. M. Reese, Y. Zhang, A fast spectral method for the boltzmann equation for monatomic gas mixtures, *J. Comput. Phys.* 298 (2015) 602–621. doi:10.1016/j.jcp.2015.06.019.
- [54] K. Aoki, Y. Sone, Y. Waniguchi, A rarefied gas flow induced by a temperature field: Numerical analysis of the flow between two coaxial elliptic cylinders with different uniform temperatures, *Comput. Math. Appl.* 35 (1) (1998) 15–28. doi:10.1016/S0898-1221(97)00255-1.
- [55] C. Geuzaine, J.-F. Remacle, Gmsh: A 3-D finite element mesh generator with built-in pre- and post-processing facilities, *Int. J. Numer. Meth. Eng.* 79 (11) (2009) 1309–1331. doi:10.1002/nme.2579.
- [56] S. Takata, M. Hattori, T. Hasebe, Slip/jump coefficients and Knudsen-layer corrections for the ES model in the generalized slip-flow theory, *AIP Conf. Proc.* 1786 (1) (2016) 040004. doi:10.1063/1.4967542.